THREE-DIMENSIONAL ACCURACY ANALYSIS OF A MAPPING-GRADE MOBILE LASER SCANNING SYSTEM

A Thesis

Presented to

the Faculty of the Department of Civil & Environmental Engineering

University of Houston

In Partial Fulfillment

of the Requirements of the Degree

Master of Science

in Geosensing Systems Engineering & Sciences

by

Darren L. Hauser

August 2013

THREE-DIMENSIONAL ACCURACY ANALYSIS OF A MAPPING-GRADE MOBILE LASER SCANNING SYSTEM

Darren L. Hauser

Approved:

Chairman of the Committee
Craig L. Glennie, Ph.D.
Assistant Professor
Civil & Environmental Engineering

Committee Members:

Ramesh L. Shrestha, Ph.D.
Hugh Roy & Lillie Cranz Cullen
Distinguished Professor
Civil & Environmental Engineering

Kenneth W. Hudnut, Ph.D.
Geophysicist
United States Geological Survey

Benjamin A. Brooks, Ph.D.
Research Geologist
United States Geological Survey

Suresh K. Khator, Ph.D.
Associate Dean
Cullen College of Engineering

Ramesh L. Shrestha, Ph.D.
Director of Geosensing Systems
Engineering & Sciences Program

Where were you when I laid the foundation of the earth?

Tell Me, if you have understanding,

Who set its measurements? Since you know.

Or who stretched the line on it?

Job 38:4-5

THREE-DIMENSIONAL ACCURACY ANALYSIS OF A MAPPING-GRADE MOBILE LASER SCANNING SYSTEM

An Abstract

of a

Thesis

Presented to

the Faculty of the Department of Civil & Environmental Engineering

University of Houston

In Partial Fulfillment

of the Requirements of the Degree

Master of Science

in Geosensing Systems Engineering & Sciences

by

Darren L. Hauser

August 2013

ABSTRACT

This thesis investigates the accuracy of a low-cost, mapping-grade mobile laser scanning system. The instruments, development, and inherent and expected errors of the system are discussed, along with the data collection techniques. The processing procedures are detailed, including the reported reliability of the post-processed results estimated by the processing algorithms.

The resulting geo-referenced pointclouds, collected in backpack mode, are compared to high-accuracy terrestrial laser scanning data. Several analysis methods are used, including planar investigations and feature extraction approaches. These techniques provide multiple perspectives on the potential accuracy of the mapping-grade system. Additionally, a high-end, survey-grade mobile laser scanning system is also utilized as a comparison standard. The final analysis showed a 6-8 cm horizontal accuracy and 4-6 cm vertical accuracy at 1σ for the mapping-grade system. It can be confidently stated that the system is able to reliably collect pointcloud data with a three-dimensional accuracy of better than ± 10 cm.

TABLE OF CONTENTS

LIST OF FIGURES

LIST OF TABLES

ANNOTATIONS

The terms, Inertial Navigation System (INS) and Inertial Measurement Unit (IMU), are occasionally used interchangeably, but their definitions should be distinguished from one another. An IMU makes raw inertial measurements using gyroscopes and accelerometers. An INS is a system that utilizes IMU data to determine the navigation trajectory of an object. In this thesis, the term INS is used to refer to a system that provides a post-processed navigation solution.

Mapping-grade and survey-grade are also designations used throughout this thesis. Mapping-grade will refer to a Mobile Laser Scanning (MLS) system utilizing a low-cost, lower-accuracy laser scanner and a tactical-grade IMU. Survey-grade will denote an MLS system with a high-end laser scanner and IMU – usually at a higher cost. For the purposes here, a mapping-grade system produces a three-dimensional point accuracy of 5-20 cm, and a survey-grade system has an accuracy of 5 cm or less, at 1σ. These descriptions are adapted from Chapter 10 of NCHRP Report 748 (Olsen et al. 2013).

The results reported in this thesis are given as 1σ values. This means that 68.3% of measurements will fall within plus or minus the stated value. To determine a larger probable error, for example 95.0%, the given value should be multiplied by 1.96, assuming a normal distribution.

1 INTRODUCTION

Terrestrial-based Mobile Laser Scanning (MLS) systems, using LiDAR (Light Detection And Ranging) technology, have been utilized for several years. Airborne Laser Scanning (ALS) has been used for even longer. These laser scanning systems map the adjacent environment with very high density by taking measurements from a moving platform. Using these techniques, a large quantity of survey data can be collected with high accuracy, in a very short period of time. These practices are in ever-increasing demand because of the extent of data recorded. Many private, public, and research disciplines use the data acquired by MLS and ALS systems.

Laser scanning from a moving platform is desirable. This is due to the large amounts of data that can be collected in a relatively short span of time, as stated above. This is an improvement over scanning from several static locations, which takes additional time for each individual setup. The downside of a mobile system, when compared to static scanning, is its lower order of accuracy. It is more accurate to use control points with known locations to solve for the origin of a single scan position than to geo-reference a moving platform, which includes several inherent errors. Clearly, for most applications, accuracy is one of the main concerns when designing and operating an MLS system.

When comparing MLS and ALS, collecting data from a ground-based or low-altitude platform is advantageous over an airborne system, because the systems are generally less expensive to operate. It is cheaper, for instance, to drive a truck than fly an airplane or helicopter. An MLS system can also collect data at higher resolutions and better accuracy because of shorter observational ranges. The challenge to these terrestrial-based systems, as hinted above, is the determination of the vehicle trajectory. Multipath and Global Navigation Satellite System (GNSS) outages, produced by buildings, underpasses, vegetation, etc., cause problems with terrestrial scanning that do not affect an airborne platform.

While the basic concepts behind mobile mapping, and more specifically MLS and ALS, have remained relatively unchanged, the systems improve as the LiDAR instruments and navigation technologies used in the systems develop. Unfortunately, this occasionally results in incomplete understanding of, and high cost for, the systems. Nevertheless, mobile mapping will remain in demand. Mobile laser scanning systems will continue to reduce workloads and increase productivity and understanding of the surrounding physical earth, nature, and infrastructure (Puente et al. 2013b).

1.1 Background

Mobile laser scanning and airborne laser scanning systems have been available for just over 10-15 years (Baltsavias 1999b, Petrie and Toth 2009c). Before this, most of the original effort in terrestrial-based mobile mapping systems concentrated on using digital cameras as the data collection instrument. Much of the initial research was accomplished at the Ohio State University and the University of Calgary. The Ohio State University's highway mapping van can be reviewed in Goad (1991) and Novak (1991). A similar concept was developed with the University of Calgary's VISAT system – for Video-Inertial-SATellite (El-Sheimy and Schwarz 1993, Schwarz et al. 1993). Both systems use GNSS receivers, Inertial Navigation Systems (INSs) or navigation instruments, and digital imaging devices to produce photogrammetric maps. Using the same notion, a mapping system using digital cameras was even implemented on a backpack (Ellum and El-Sheimy 2002).

Today, mobile systems are becoming more popular, especially those incorporating LiDAR instruments. In reality, the shift from digital cameras to laser scanners is simple; the navigation systems are the complex aspect of mobile mapping. Several of the earliest, innovative GNSS/INS platforms using cameras and laser range finders are mentioned Grejner-Brzezinska

(2001). However, one of the first true MLS systems was developed in 2003 by installing an airborne LiDAR instrument on a truck (Olsen et al. 2013). The initial development and testing is discussed in Newby and Mrstik (2005). Petrie and Toth (2009c) and Puente et al. (2013b) review many current commercial and research MLS systems, including the systems' lasers, navigation equipment, and other integrated sensors. Like most present technology, these systems have advanced rapidly in less than 25 years.

Airborne mapping systems were in use well before terrestrial-based LiDAR systems. Airborne laser scanning-related technology began during the 1960s and 1970s with laser profiling systems, and then advanced to actual scanning a few years later (Petrie and Toth 2009a). These ALS instruments are usually operated from small aircraft or helicopters. Satellite platforms exist as well, but will not be discussed here. There are many systems available for collecting airborne data, and several manufacturers and operators are reviewed in Guenther (2007) and Petrie and Toth (2009a). Recently, as equipment size and weight decreases, laser scanning systems are beginning to be designed for Unmanned Aerial Vehicles (UAVs), as presented by Nagai et al. (2009) and Wallace et al. (2012). Adaptable systems, for use on a variety of MLS or ALS platforms, have been developed as well (Glennie et al. 2013, Jaakkola et al. 2010).

The accuracy and performance of an MLS or ALS system is very important for it to be practical. Validation of mapping systems has been undertaken using several methods. Focusing only on the more recent MLS technology, planar patches from MLS system pointclouds have been compared to existing models and found to agree within several centimeters (Haala et al. 2008). Investigations comparing pointclouds with static and Real-Time Kinematic (RTK) GNSS control points were examined by Barber et al. (2008) and Hunter et al. (2006), with elevation agreements of 3-4 cm and horizontal agreements of ± 10 cm, and elevation agreements of ± 2 cm, respectively. Similarly, ground features surveyed by RTK GNSS, leveling, and total station

were used in Glennie (2009). Finally, centimeter-level relative accuracies of MLS systems, between multiple flightlines, were briefly explored by Barber et al. (2008) and Puente et al. (2013a). A detailed three-dimensional error analysis and comparison was conducted by Glennie (2007) to assess the potential accuracy of MLS systems. These methods, along with many other studies, have validated the accuracy of data collected by MLS systems.

High accuracy allows the use of the technology for many applications. Therefore, there are numerous and varying uses for LiDAR data collected from a mobile platform. Some uses include archaeology and canopy penetration (Chase et al. 2011, Devereux et al. 2005), topographical changes using MLS (Vaaja et al. 2011) and ALS (Shrestha et al. 2005), and fault detection and measurements (Brooks et al. n.d., Carter et al. 2007). Other various geomorphological uses, like landslide detection and sinkhole location, are discussed in Carter et al. (2001) and Carter et al. (2007). Likewise, bathymetry for hydrographic and near-shore mapping is a related and popular discipline (Guenther 2007).

Engineering projects such as corridor mapping, roadway analysis, as-built surveys, and slope stability studies, as seen in the last part of Lindenbergh (2010) and Olsen et al. (2013), are an additional important focus of MLS and ALS. Projects such as assessing solar potential (Jochem et al. 2011) and monitoring corridor rockfalls (Lato et al. 2009) are possible with MLS, along with tree and pole feature extraction (Jaakkola et al. 2010). The area of kinematic laser scanning research and development is certainly a multi-disciplinary field, with uses far beyond those mentioned.

1.2 Theory

Mobile LiDAR systems use the same theories and similar instrumentation whether they are terrestrial-based or airborne. The most basic equipment needed for an MLS system includes

a scanner, a GNSS antenna and receiver, and an INS. The scanner records Cartesian coordinates for points on the surfaces of surrounding objects. These coordinates are in an arbitrary system relative to the scanner itself, often referred to as the Scanner's Own Coordinate System (SOCS). The GNSS receiver and INS instrument provide positioning in the global and body system, respectively. Data from the three instruments are integrated, resulting in a globally georeferenced pointcloud. Along with processing software, this is enough to provide the user with real-world positioning of a mapped location.

1.2.1 Laser Scanners

The laser scanner, or LiDAR instrument, is the piece of equipment that actually images the surrounding environment. As mentioned previously, data points from object surfaces are referenced in the SOCS. These points are measured using a range and angle from the scanner's origin. Unsurprisingly, the scanning instrument uses a laser to measure distance to an object.

The term laser denotes Light Amplification by Stimulated Emission of Radiation. In other words, a laser emits electromagnetic radiation (EMR), or light, when activated by an energy source. This technology was introduced c. 1960 (Hecht 2010).The resulting EMR is very collimated and acts as a directional pulse or beam (Petrie and Toth 2009b). This characteristic allows the range from the instrument to an object to be precisely measured – hence the designation LiDAR.

Since the instrument produces the energy needed to record an observation, a laser scanner is an active sensor. This is in contrast to a passive sensor. An example of a passive sensor is a camera; the light used to take a photograph comes from an outside source like the sun. Unlike a camera, an active sensor, like a laser scanner, can be used in any lighting condition.

There are two typical approaches a laser scanner uses to determine range: time-of-flight (TOF) or continuous-wave (CW). A TOF, or pulsed, instrument determines the precise time for a

short pulse of EMR to travel from the scanner to an object and back to the scanner (see Figure 1). From the calculated time, a range is solved by

$$R = \frac{ct}{2}, \tag{1}$$

where

c is the known speed of EMR, and

t is the total travel time of the pulse.

It may be necessary to apply a constant to c to account for the medium the EMR is traveling through (Beraldin et al. 2010).

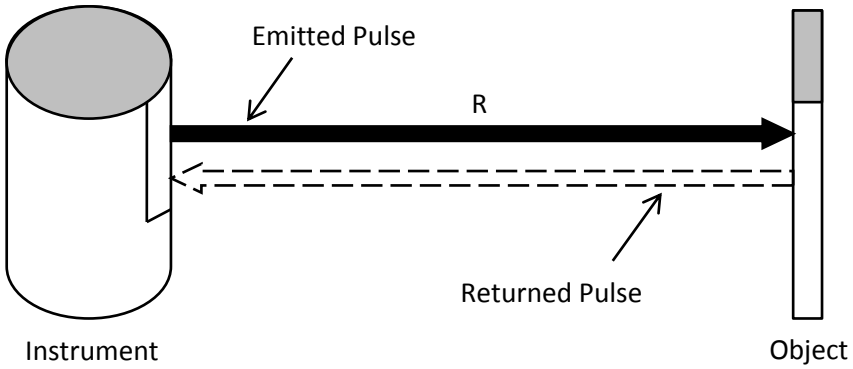

Figure 1: Operation of a time-of-flight instrument

A CW, or phase-based, instrument emits a continuous beam of EMR and determines the precise phase difference between the emitted beam and returned beam. These instruments are often more accurate than TOF instruments but have a shorter ranging capability. This category of instrument will not be reviewed further, as it was not used in this research.

Additionally, to solve for the actual coordinates (x, y, z) of a point, an angle must be calculated. This includes a horizontal and/or vertical angle. With an angle and range from the instrument's axes and measurement reference point, the coordinates for a point on an object can be determined in the SOCS using coordinate geometry and basic trigonometry. This topic will be covered further, with specific laser scanners, in Section 2.1.1 and 2.2.1.

1.2.2 Navigation Systems

The navigation system provides the position and orientation information needed to reference the moving platform to a global or local coordinate system. The navigation system of an MLS platform includes both GNSS and Inertial Measurement Unit (IMU) components. The GNSS determines the location of the MLS system using satellite positioning, while the IMU determines its orientation.

An IMU contains inertial sensors called gyroscopes and accelerometers. Gyroscopes measure the rate of angular change of a system with respect to inertial space. Accelerometers record the specific force applied to the system; this is along the sensitive axes of the accelerometer (Groves 2008).

As the mapping platform moves, it is subjected to rotational and specific forces from platform motion. The IMU provides orientation in roll (ω), pitch (φ), and heading (κ) using the gyroscopes and accelerometers. The orientation, or attitude, values are the rotations about the *x*-, *y*-, and *z*-axes of the mapping platform (see Figure 2).

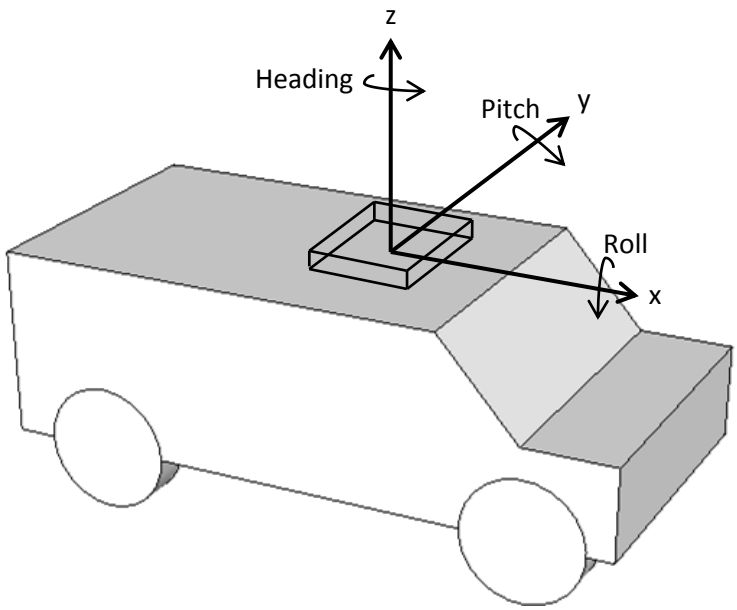

Figure 2: Rotations and axes of a mobile mapping platform

As stated, GNSS and INS components are both present. The GNSS and INS are complimentary systems. Since GNSS can undergo outages and blocked signals, IMU measurements are used to determine changes in position and the orientation when the GNSS is not receiving satellite signals. Because an INS suffers from positioning errors over time, the GNSS is utilized to regularly update the INS's position. This is demonstrated in Figure 3. When a GNSS outage occurs, the error in position increases rapidly until satellite signal is regained. In other words, an INS has little noise in the short-term, but its error increases significantly with time, and GNSS is noisier during short periods but is accurate in the long-term.

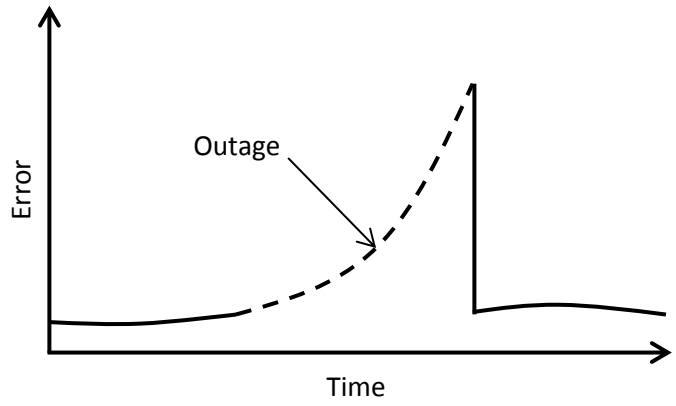

Figure 3: Error in position over time due to GNSS outage

To optimally determine position and orientation, a Kalman Filter (KF) is used. When a GNSS/INS is implemented with a laser scanner, this step is usually done post-collection. A basic KF takes available measurements or information about a system or process and estimates a current value for the variables in question, so the errors are statistically minimized (Maybeck 1979). Simply, the KF utilizes the system's measurements as updates to predict the position, orientation, and errors of the system at a present state. This is a recursive process.

Additionally, a KF can be expanded to include smoothing to improve the results (Groves 2008). Smoothing is used because the KF is based on predictions, and when a GNSS signal is blocked, the INS will quickly degrade, as previously stated. Forward-and-backward smoothing is normally used in MLS applications. In this case, the KF is run forward and backward independently. The final estimate is a combination of the two filters. As shown in Figure 4, final accuracy can be greatly improved by applying the KF in forward and backward directions. This smooths the data and gives a better approximation of the state of the system at each epoch of time.

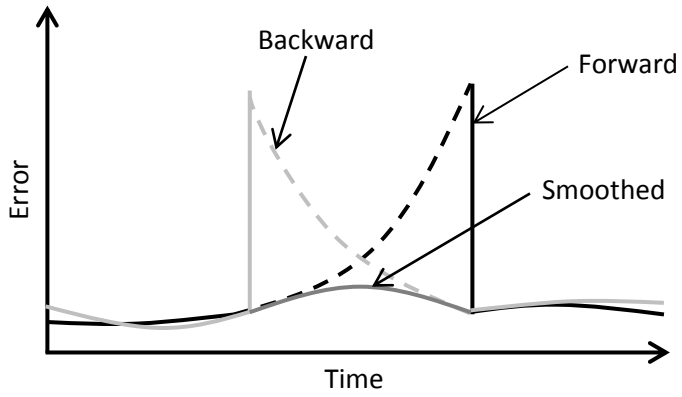

Figure 4: Forward-and-backward smoothing by Kalman filter

1.2.3 System Integration

By integrating the kinematically collected data from the laser scanner and GNSS/INS, the coordinates of points on an object can be calculated. The geo-referenced coordinate of a point in a global coordinate system, given by Glennie et al. (2013), is

$$p_G^l = p_{GNSS}^l + R_b^l\left(R_s^b \cdot p^s - l^b\right), \tag{2}$$

where

p^l_{GNSS} is the coordinate value of the navigation sensor origin in the global frame,

R^l_b is a rotation matrix from the body (b) frame to the local-level (l) frame,

R^b_s is a rotation matrix from the scanner (s) frame to the b-frame,

p^s is the coordinate of a point in the s-frame, and

l^b is the offset between the b-frame and s-frame, given in the b-frame.

The l-frame is a navigation reference for the GNSS/INS, where the axes point north, east, and up or down (Lichti and Skaloud 2010). The b-frame is the frame of reference of the INS sensor, and the s-frame is the arbitrary SOCS used by the scanner. This is demonstrated in Figure 5, keeping in mind the concepts from Figure 2.

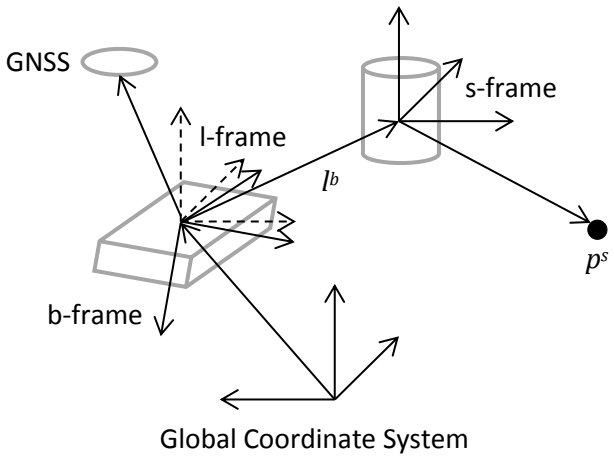

Figure 5: Geo-referencing of a laser scanner point

In order to rotate from the b-frame to the l-frame, ω, φ, and κ are required. As stated, these are the rotation values the INS estimates. Obviously, these variables are always changing with the platform's movements and must be updated with respect to time. To rotate from the s-frame to the b-frame, boresight angles are needed; this is the boresight matrix. The boresight is the angular offset between the SOCS and the INS's coordinate system. The angles are constant throughout a survey. They are calculated with a boresight calibration, which can be done manually, or with a statistical adjustment. Manual calibration involves manually changing the boresight and subsequently reprocessing the data, until the pointcloud is visually correct. A rigorous calibration includes statistically adjusting points on planar surfaces to determine the boresight values (e.g., Glennie (2012) and Rieger et al. (2010) for MLS systems). Finally, the offset between the b-frame and s-frame is the lever-arm offset. This is the measured difference, or positional offset, of the origins of the two frames (see Figure 6).

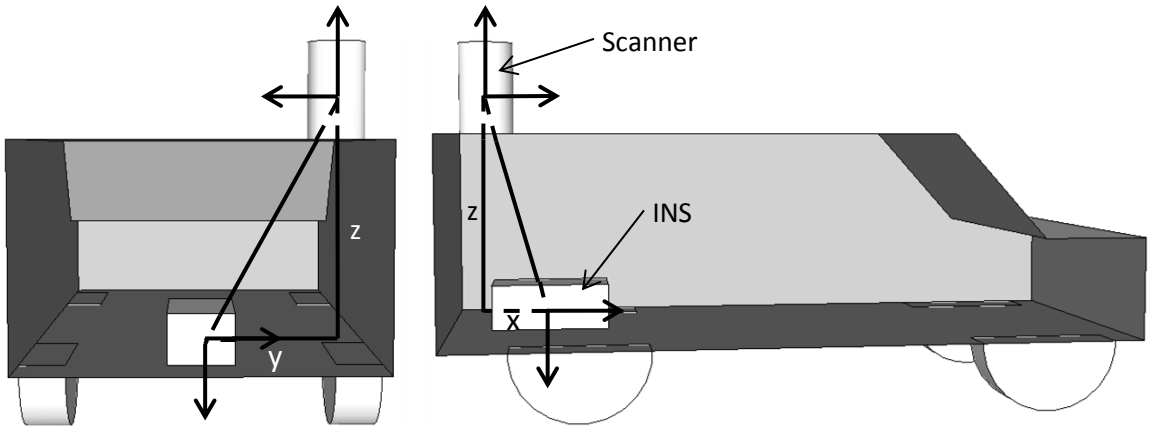

Figure 6: Lever-arm offset between INS and laser scanner

1.3 Research Objectives

Dozens of terrestrial MLS and ALS systems have been built in the past several years. Generally, these systems have several disadvantages. They are usually expensive (> $250K), large, and can be complex to operate. When a system is assembled, it is often used on only one particular platform, because switching between platforms is involved and becomes impractical and time consuming. These limitations demand valuable user resources and offer reduced operational versatility. It is also difficult to use many of these systems in delicate areas or remote locations, since operation is intrusive and access is limited.

Systems containing small LiDAR instruments have been constructed in an attempt to resolve these shortcomings (e.g., Jaakkola et al. (2010)). Many of these systems, however, are comprised of lower-accuracy sensors that cause diminished pointcloud accuracy. Thus, they cannot meet the demanding requirements of numerous applications. Most recently, Brooks et al. (n.d.) and Glennie et al. (2013) proposed a low-cost (< 100K), mapping-grade system that attempts to solve the limitations posed by other systems by using upgraded laser scanning and navigation sensors. It was developed to meet many engineering, Earth science, and topographic

applications. The MLS system is compact, while still aiming to meet required accuracy levels of < 10 cm vertical and < 20 cm horizontal.

With compact and inexpensive MLS systems now operational, the accuracy levels of these systems are in question. Often, data collected from MLS systems are only compared to "true" coordinates collected through conventional methods, like GNSS or total station surveys. However, little significant research has been completed using an MLS versus Terrestrial Laser Scanning (TLS) evaluation. Brief comparisons using surface models have been done between the two methods in Glennie (2009), Glennie et al. (2013), and Vaaja et al. (2011), while planar comparison methods were used with success in Glennie et al. (2013) and Yen et al. (2010). Also, evaluations have been made with practical uses, as demonstrated by forestry investigations in Lin et al. (2010) and Lin et al. (2011) and erosion studies in Young et al. (2010).

Terrestrial laser scanning is significant because data collected by TLS is of high accuracy. Normally, it is assumed that TLS data will be of higher quality than MLS data. Using TLS data as control is desirable because of the high density of its coverage. This would assist in showing MLS accuracy over greater areas of data, rather than at single positions, as many other approaches attempt. Confidence in MLS system accuracy would then be strengthened.

The techniques used in this research for analyzing MLS pointclouds with TLS control included numerous planar patch comparisons and multiple feature extraction evaluations. How will several of these comparison techniques relate? Do methods like point-to-plane and point-to-point analysis produce similar results? How do specific targets like cylindrical objects and linear features relate between MLS and TLS pointclouds?

In addition, since several survey-grade MLS systems have been created, explored, and verified by others, it would be advantageous to investigate the comparisons between a mapping-grade and survey-grade system. Some additional questions are necessary. How equivalent

are systems with LiDAR and INS instruments of differing quality? How do the resulting point-clouds of both systems compare? Moreover, does the accuracy of the mapping-grade system ultimately enable it to be used in the same situations as a survey-grade system?

This thesis will answer the above questions. Different methods of comparison will be used to analyze the mapping-grade MLS data. Static TLS and survey-grade MLS data will be utilized as control. Finally, the expected three-dimensional accuracy of the low-cost, mapping-grade MLS system will be quantified.

2 RESEARCH MLS SYSTEMS

Two MLS systems were used for this research. The first was a mapping-grade system, and the second a survey-grade system. The survey-grade system consisted of some of the best laser scanning and navigation equipment currently available. The mapping-grade system utilized equipment with mid-grade specifications, and of a significantly reduced cost and weight, compared to the survey-grade system.

2.1 Mapping-Grade MLS System

2.1.1 Instrumentation

The mapping-grade system utilized a Velodyne HDL-32E scanner (see Figure 7). The scanner features 32 lasers aligned vertically, producing a 40° field-of-view, and scans 360° horizontally. The HDL-32E uses a low-cost GNSS receiver for time-stamping its recorded data.

Figure 7: Velodyne HDL-32E Laser Scanner
(© Velodyne Lidar, Inc.)

The Velodyne scanner is much smaller, lighter, and consumes less power when operating, than the survey-grade scanner, which will be discussed in Section 2.2.1. This makes it ideal for use on a compact mapping platform. Unfortunately, these factors also lead it to be significantly less accurate. Table 1 presents the manufacturer's specifications for the Velodyne HDL-

32E. As can be seen, the instrument has a high measurement rate, due to the 32 lasers and rotating head, with which to image its surroundings.

Table 1: Velodyne HDL-32E manufacturer specifications

Dimensions (cm)	ø 8.5 × 14.4
Weight (kg)	2.0
Laser Wavelength (nm)	905
Beam Divergence (mrad)	2.79
Typical Ranging Ability (m)	70
Accuracy (mm)	20 [@ 25 m]
Angular Resolution (hz°/vt°)	0.16/1.33
Measurement Rate (kHz)	700
Power Consumption (W/V DC)	24/9-32

The Velodyne scanner computes coordinates in the SOCS using the equation presented by Glennie and Lichti (2010) as

$$p^s = \begin{bmatrix} x \\ y \\ z \end{bmatrix} = \begin{bmatrix} (s \cdot R + D_o) \cdot cos(\alpha) \cdot [sin(\varepsilon)\, cos(\beta) - cos(\varepsilon)\, sin(\beta)] - H_o \cdot [cos(\varepsilon)\, cos(\beta) + sin(\varepsilon)\, sin(\beta)] \\ (s \cdot R + D_o) \cdot cos(\alpha) \cdot [cos(\varepsilon)\, cos(\beta) + sin(\varepsilon)\, sin(\beta)] + H_o \cdot [sin(\varepsilon)\, cos(\beta) - cos(\varepsilon)\, sin(\beta)] \\ (s \cdot R + D_o) \cdot sin(\alpha) + V_o \end{bmatrix}, \quad (3)$$

where

s is the distance scale factor,

D_o is the distance offset from the scanner origin,

α is the correction for vertical rotation,

β is the correction for horizontal rotation,

H_o is the horizontal offset from the scanner origin,

V_o is the vertical offset from the scanner origin,

R is the range measurement, and

ε is the encoder angle measurement.

The first six factors are calibration values particular to each instrument and specific to each of the 32 individual lasers. The last two parameters are the raw observations provided by the instrument from each of the 32 lasers.

Next, the tactical-grade INS was an Oxford Technical Solutions (OxTS) Inertial+2 (see Figure 8). It is the largest sensor in the mapping-grade system. Heading is difficult to determine for an INS, especially a tactical instrument, so the system uses two GNSS antennas to assist in heading determination, as well as two high-quality external receivers for positioning. An internal L1 receiver is also present to time-stamp the measurements.

Figure 8: OxTS Inertial+2 Navigation System

The Inertial+2 is small and lightweight (see Table 2). It uses Micro-Electro-Mechanical System (MEMS) technology for its IMU instrumentation. The technology of MEMS relies on special manufacturing materials and techniques to produce an advanced product. This means that the components are small and inexpensive to build (Titterton and Weston 2004). The OxTS Inertial+2 includes three gyroscopes and three accelerometers for its MEMS inertial sensors.

Table 2: OxTS Inertial+2 manufacturer specifications

Dimensions (cm)	23.4 × 12.0 × 8.0
Weight (kg)	2.2
Roll/Pitch Accuracy (°)	0.03
Heading Accuracy (°)	0.1
Gyro Bias ($°/_h$)	2
Accelerometer Bias (mg)	∼1
Measurement Rate (Hz)	100
Power Consumption (W/V DC)	15/9-18

Finally, the external GNSS receivers and antennas for positioning were NovAtel FlexPak6s and Antcom G5Ant-52AT1s, respectively. The small receiver has dimensions of only 14.7 × 11.3 × 4.5 cm and weighs just over 0.3 kg. This has a measurement and output rate of up to 100 Hz, a measurement precision of 1 mm or less, and a time accuracy of 20 ns. The receiver has the ability to track multiple bands and multiple constellations of satellites. The antenna measures ø 12.7 × 4.3 cm and weighs only 0.2 kg.

2.1.2 Configuration

Part of the original goal in designing a compact system was to provide adaptable mapping ability. The mapping-grade MLS system can be configured in several different ways and has been tested on multiple platforms. The system has been operated using a vehicle, backpack, and weather balloon as the mobility platform. Before development started, the system was tested in vehicle mode. This configuration is stable and minimizes INS errors due to swaying or heaving motion, and verified that the system could viably collect data.

Next, an instrument pod was designed, and the system was installed on a weather balloon (see Figure 9). This offers a way to perform low-altitude mobile scanning. In this configuration, the instrument pod is tethered to a 14-ft diameter, helium-filled balloon. Mapping is

performed by towing the system behind a vehicle or manually walking it using secured tether lines (Glennie et al. 2013).

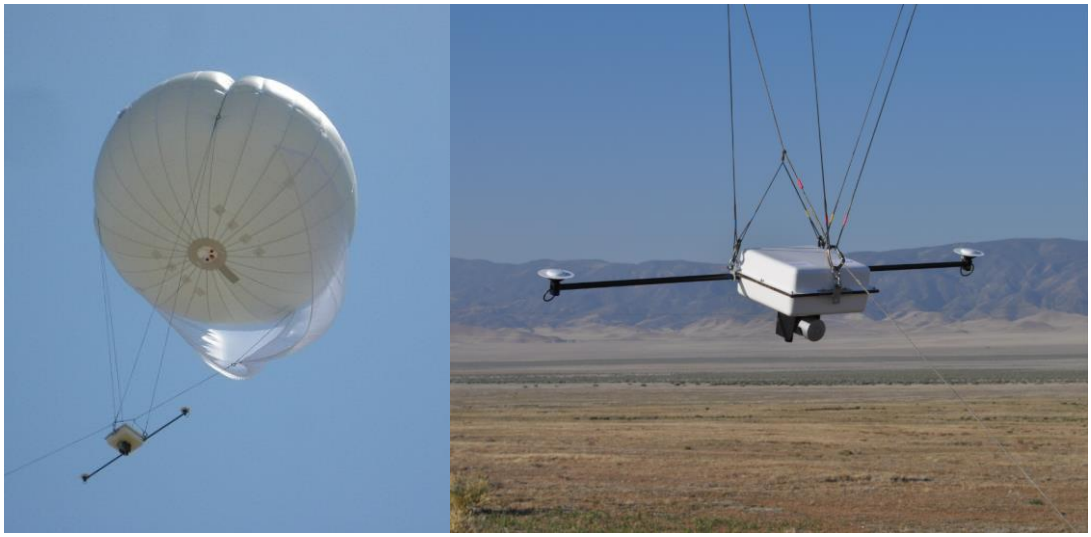

Figure 9: Balloon configuration for the mapping-grade MLS system

Furthermore, the backpack platform is shown in Figure 10. This configuration offers a highly flexible option for mapping and is ideal for areas where a large vehicle cannot gain access. An arrangement such as this would also provide an optimal way to perform indoor mapping. The backpack configuration was used for the data collection presented herein.

Figure 10: Backpack configuration for the mapping-grade MLS system

The system's instrument pod can be seen in Figure 11. The pod provides a stable platform from which the data collection instruments can operate while remaining fixed in relation to one another. It consists of a Velodyne interface box, lithium-ion batteries, power distributer, and tablet computer. The interface box integrates Ethernet control, power, and GNSS antenna input for the Velodyne scanner. The batteries provide ample power to run the system for several hours, and the tablet computer controls all of the sensors. The bottom portion of the pod contains the Inertial+2 INS and GNSS receivers.

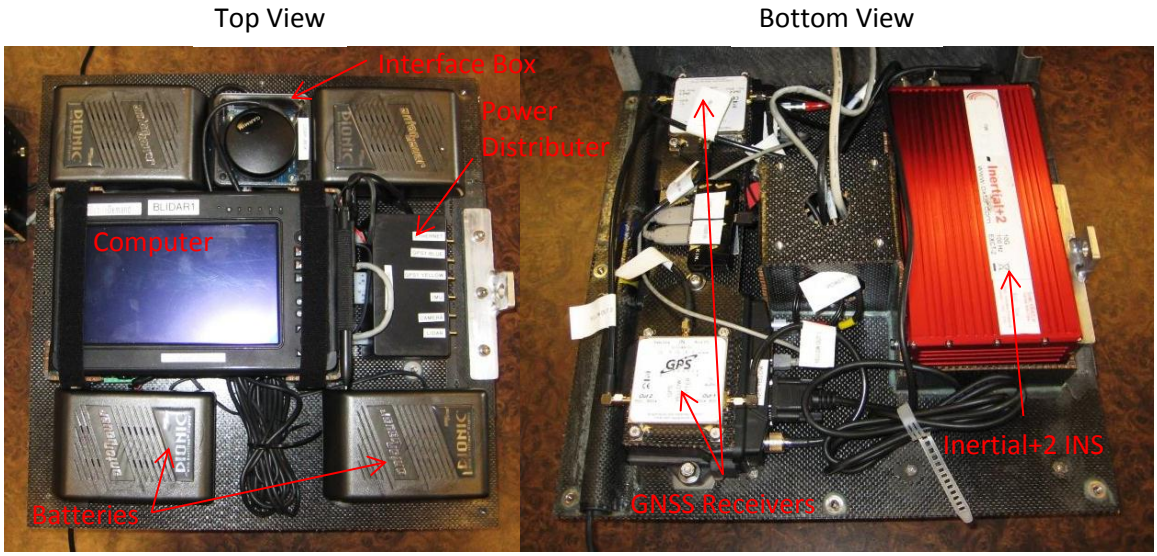

Figure 11: Compact instrument pod for the mapping-grade MLS system

The Velodyne scanner and GNSS antennas are attached to the exterior of the pod (see Figure 10). A small digital camera is also mounted below the laser scanner, and a second external GNSS receiver is present, but these will not be used in this analysis. The total weight of the system is approximately 15 kg.

2.1.3 Error Budget

All instruments and measurements contain systematic, random, temporal, or static run-to-run errors, and the mapping-grade system is no exception. For instance, Velodyne-specific

errors are covered in Glennie and Lichti (2010) and Glennie and Lichti (2011), while general LiDAR instrument and observational errors in pointclouds are reviewed in Boehler et al. (2003) and Lichti et al. (2005). Errors in GNSS, such as clock biases, atmospheric effects, and multipath, are discussed by Hofmann-Wellenhof et al. (2008), and additionally in Groves (2008). Constant error characteristic of gyroscope and accelerometer sensors, IMU axes misalignment, and total INS errors can also be found in Groves (2008), and the errors in integrated systems are discussed with detail in Baltsavias (1999a) and Morin (2002). As can be seen, dozens of internal and external errors and effects will be present in the MLS observations, causing noticeable uncertainty.

Therefore, a simple error analysis was completed to estimate the expected three-dimensional point accuracy of the mapping-grade MLS system. This estimation is dependent on 20 parameters. Expanding Equation 2 to include variables from the GNSS/INS and terms from the Velodyne equation produces

$$\begin{bmatrix} X \\ Y \\ Z \end{bmatrix}_G^l = \begin{bmatrix} X \\ Y \\ Z \end{bmatrix}_{GNSS}^l + R_b^l(\omega \quad \varphi \quad \kappa) \cdot \left(R_s^b(d\omega \quad d\varphi \quad d\kappa) \cdot p^s(s \quad D_o \quad \alpha \quad \beta \quad H_o \quad V_o \quad R \quad \varepsilon) - \begin{bmatrix} l_x \\ l_y \\ l_z \end{bmatrix}^b \right). \quad (4)$$

Mimicking the method used by Glennie (2007), the system error formula can be solved by linearizing the Equation 4 using a Taylor series expansion, truncated after the first term. The differential equation is

$$\begin{bmatrix} \delta X \\ \delta Y \\ \delta Z \end{bmatrix}_G^l = \begin{bmatrix} \delta X \\ \delta Y \\ \delta Z \end{bmatrix}_{GNSS}^l + A \begin{bmatrix} \delta\omega \\ \delta\varphi \\ \delta\kappa \end{bmatrix} + B \begin{bmatrix} \delta d\omega \\ \delta d\varphi \\ \delta d\kappa \end{bmatrix} + C \begin{bmatrix} \delta s \\ \delta D_o \\ \delta\alpha \\ \delta\beta \\ \delta H_o \\ \delta V_o \\ \delta R \\ \delta\varepsilon \end{bmatrix} + D \begin{bmatrix} \delta l_x \\ \delta l_y \\ \delta l_z \end{bmatrix}, \quad (5a)$$

where A, B, C, and D are Jacobian matrices containing the partial derivatives of the point coordinate taken with respect to each error. They are given as

$$A = \begin{bmatrix} \frac{\partial X_G^l}{\partial \omega} & \frac{\partial X_G^l}{\partial \varphi} & \frac{\partial X_G^l}{\partial \kappa} \\ \frac{\partial Y_G^l}{\partial \omega} & \frac{\partial Y_G^l}{\partial \varphi} & \frac{\partial Y_G^l}{\partial \kappa} \\ \frac{\partial Z_G^l}{\partial \omega} & \frac{\partial Z_G^l}{\partial \varphi} & \frac{\partial Z_G^l}{\partial \kappa} \end{bmatrix}, \; B = \begin{bmatrix} \frac{\partial X_G^l}{\partial d\omega} & \frac{\partial X_G^l}{\partial d\varphi} & \frac{\partial X_G^l}{\partial d\kappa} \\ \frac{\partial Y_G^l}{\partial d\omega} & \frac{\partial Y_G^l}{\partial d\varphi} & \frac{\partial Y_G^l}{\partial d\kappa} \\ \frac{\partial Z_G^l}{\partial d\omega} & \frac{\partial Z_G^l}{\partial d\varphi} & \frac{\partial Z_G^l}{\partial d\kappa} \end{bmatrix},$$

$$C = \begin{bmatrix} \frac{\partial X_G^l}{\partial s} & \frac{\partial X_G^l}{\partial D_o} & \frac{\partial X_G^l}{\partial \alpha} & \frac{\partial X_G^l}{\partial \beta} & \frac{\partial X_G^l}{\partial H_o} & \frac{\partial X_G^l}{\partial V_o} & \frac{\partial X_G^l}{\partial R} & \frac{\partial X_G^l}{\partial \varepsilon} \\ \frac{\partial Y_G^l}{\partial s} & \frac{\partial Y_G^l}{\partial D_o} & \frac{\partial Y_G^l}{\partial \alpha} & \frac{\partial Y_G^l}{\partial \beta} & \frac{\partial Y_G^l}{\partial H_o} & \frac{\partial Y_G^l}{\partial V_o} & \frac{\partial Y_G^l}{\partial R} & \frac{\partial Y_G^l}{\partial \varepsilon} \\ \frac{\partial Z_G^l}{\partial s} & \frac{\partial Z_G^l}{\partial D_o} & \frac{\partial Z_G^l}{\partial \alpha} & \frac{\partial Z_G^l}{\partial \beta} & \frac{\partial Z_G^l}{\partial H_o} & \frac{\partial Z_G^l}{\partial V_o} & \frac{\partial Z_G^l}{\partial R} & \frac{\partial Z_G^l}{\partial \varepsilon} \end{bmatrix}, \text{ and } D = \begin{bmatrix} \frac{\partial X_G^l}{\partial l_x} & \frac{\partial X_G^l}{\partial l_y} & \frac{\partial X_G^l}{\partial l_z} \\ \frac{\partial Y_G^l}{\partial l_x} & \frac{\partial Y_G^l}{\partial l_y} & \frac{\partial Y_G^l}{\partial l_z} \\ \frac{\partial Z_G^l}{\partial l_x} & \frac{\partial Z_G^l}{\partial l_y} & \frac{\partial Z_G^l}{\partial l_z} \end{bmatrix}. \quad \text{(5b)}$$

The estimated errors used for the instrument parameters $\delta\omega$, $\delta\varphi$, $\delta\kappa$, δR, and $\delta\varepsilon$ were the previously given manufacturers' values (see Table 1 and Table 2). The errors in the boresight angles were anticipated to be the same as the approximation by least-squares quantities used in Glennie (2007), and the estimates from the GNSS and lever-arm were reasonable approximations given knowledge of the system. All the estimated errors can be found in Table 3. The internal Velodyne parameters were optimistic values but accepted nonetheless.

Table 3: Estimated errors of mapping-grade MLS parameters

Parameter	**X (m)**	**Y (m)**	**Z (m)**	**ω (°)**	**φ (°)**	**κ (°)**	**dω (°)**	**dφ (°)**	**dκ (°)**	**s**
Error	0.02	0.02	0.03	0.03	0.03	0.1	0.001	0.001	0.004	0.001
Parameter	**D_o (m)**	**α (°)**	**β (°)**	**H_o (m)**	**V_o (m)**	**R (m)**	**ε (°)**	**l_x (m)**	**l_y (m)**	**l_z (m)**
Error	0.002	0.020	0.020	0.002	0.002	0.02	0.016	0.02	0.01	0.02

Solving Equation 5, given the estimated errors and likely parameters, provided the potential accuracy level of the system. The mapping-grade MLS system should perform with a three-dimensional accuracy of ± 15.5 cm at 10 m range to target. However, it is expected that the system can perform better than this, when acknowledging the initial results presented by Glennie et al. (2013), since the accuracy was reported to be at approximately this level or less.

Furthermore, the accuracy of an MLS system is dependent on the range to a target (Glennie 2007). To understand this effect, the expected error with respect to range was plotted

for the mapping-grade system (see Figure 12). As can be observed, the system has the potential to suffer a significant decrease in accuracy throughout the normal LiDAR instrument ranging capability. The thesis analysis will determine the realistic level of the system uncertainties considering the entire extent of ranges.

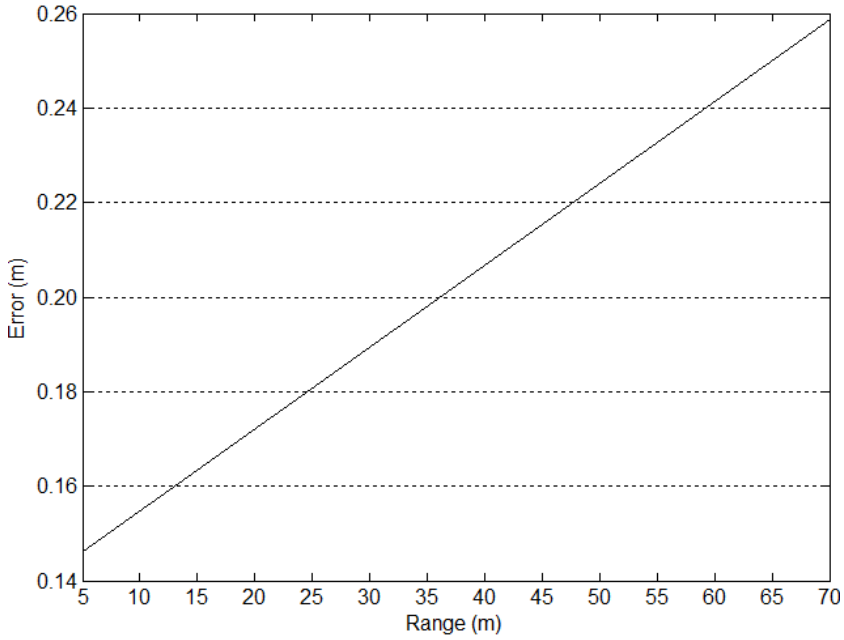

Figure 12: Expected error of mapping-grade MLS system with respect to range

2.2 Survey-Grade MLS System

2.2.1 Instrumentation

The laser scanner used for the survey-grade system was a RIEGL VZ-400 (see Figure 13). The VZ-400 operates with a single, near-infrared laser. The instrument has the ability to scan 360° horizontally and has a 100° vertical field-of-view using a polygonal, rotating mirror. It also functions in a vertical line mode for use in mobile scanning.

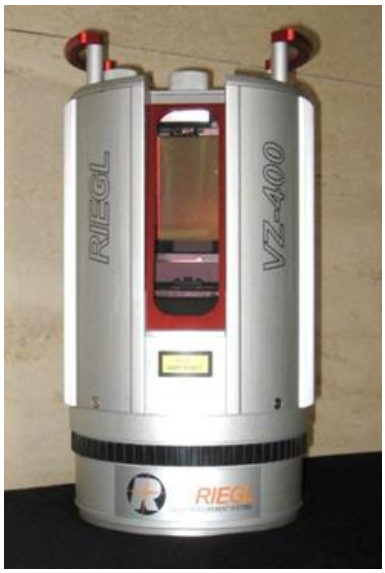

Figure 13: RIEGL VZ-400 Laser Scanner

The instrument itself is small and lightweight, when compared to many surveying laser scanners, but still too large to be implemented on a very compact platform. Its specifications are given in Table 4, and the Velodyne HDL-32E specifications are repeated for comparison. As can be seen, the VZ-400 is a much larger, but more accurate, instrument. Its range measurement accuracy is over four times better than the HDL-32E. The RIEGL's minimum potential resolution between laser shots is much smaller, but the Velodyne instrument can collect data at more than twice the rate.

Table 4: Laser scanner manufacturer specifications

	RIEGL VZ-400	Velodyne HDL-32E
Dimensions (cm)	ø 10.8 × 30.8	ø 8.5 × 14.4
Weight (kg)	9.6	2.0
Laser Wavelength (nm)	1550	905
Beam Divergence (mrad)	0.35	2.79
Typical Ranging Ability (m)	350	70
Accuracy (mm)	5 [@ 100 m]	20 [@ 25 m]
Angular Resolution (hz°/vt°)	0.0024/0.0024	0.16/1.33
Measurement Rate (kHz)	300	700
Power Consumption (W/V DC)	65/11-32	24/9-32

The RIEGL scanner computes coordinates in the SOCS by

$$p^s = \begin{bmatrix} x \\ y \\ z \end{bmatrix} = \begin{bmatrix} R\sin(\theta)\cos(\phi) \\ R\sin(\theta)\sin(\phi) \\ R\cos(\theta) \end{bmatrix}. \quad (6)$$

Here,

R is the range measurement,

θ is the zenith angle of the laser beam created by the rotating mirror, and

ϕ is the horizontal angle from the horizontal encoder measurement.

For the survey-grade MLS system, the instrument scanned in vertical line mode where $y \approx 0$ in the SOCS. The slight discrepancy in the coordinate originates from a factory calibration. In this thesis, the VZ-400 was also used to collect the TLS control pointcloud data. In the static instance, the scanner rotates 360° horizontally, and a cylindrical field-of-view is generated around the instrument, optimizing its coverage.

The survey-grade system INS was an iXSea LANDINS (see Figure 14). It is twice the size and weight, and about an order of magnitude more accurate than the OxTS Inertial+2. It can measure roll, pitch, and heading with a measurement rate of up to 200 Hz.

Figure 14: iXSea LANDINS Navigation System

The LANDINS is a relatively bulky and heavy instrument (see Table 5). This is due to its sensors, which are much larger than the MEMS sensors of the Inertial+2. Its IMU includes three highly accurate fiber optic gyroscopes and three pendulous accelerometers. The LANDINS also contains an internal Trimble multi-band GNSS receiver board for positioning and data time-stamping. The external antenna used by the system was a Trimble Zephyr Model 2. It measures ø 16.5 × 7.6 cm and weighs 0.5 kg.

Table 5: Navigation system manufacturer specifications

	iXSea LANDINS	**OxTS Inertial+2**
Dimensions (cm)	27.5 × 13.6 × 17.5	23.4 × 12.0 × 8.0
Weight (kg)	4.5	2.2
Roll/Pitch Accuracy (°)	0.005	0.03
Heading Accuracy (°)	0.01	0.1
Gyro Bias ($°/_h$)	0.005	2
Accelerometer Bias (mg)	0.02	~1
Measurement Rate (Hz)	200	100
Power Consumption (W/V DC)	18/12-32	15/9-18

2.2.2 Configuration

An aluminum plate was designed and machined to fit the VZ-400 and LANDINS instruments (see Figure 15). This allowed the sensors to stay fixed in orientation and position with respect to one another; precision machining guaranteed the axes of the instruments were as close to orthogonal as possible. The plate contains a bracket oriented directly over the INS measurement center for a GNSS antenna. By confining the offset between the GNSS and INS to only one direction, any errors in this lever-arm are minimized. Additionally, the antenna is located above the other instruments to minimize GNSS signal multipath.

Figure 15: Configuration for the survey-grade MLS system

Although bulky, the plate can be used on a vehicle or cart, while maintaining the same configuration. This provides more options depending on the application. A cart, for example, would allow better access to areas where maneuvering a car would be more difficult. Meanwhile, a vehicle could survey large areas at high speeds, saving valuable time. For the data collection included within, a cart was used for mobility.

3 DATASETS

The mapping-grade MLS research data was collected on January 26 and January 31, 2103, at the University of Houston's Energy Research Park (see Figure 16). This location provided ample room to operate. More importantly, many planar surfaces at varying object ranges and orientations were present.

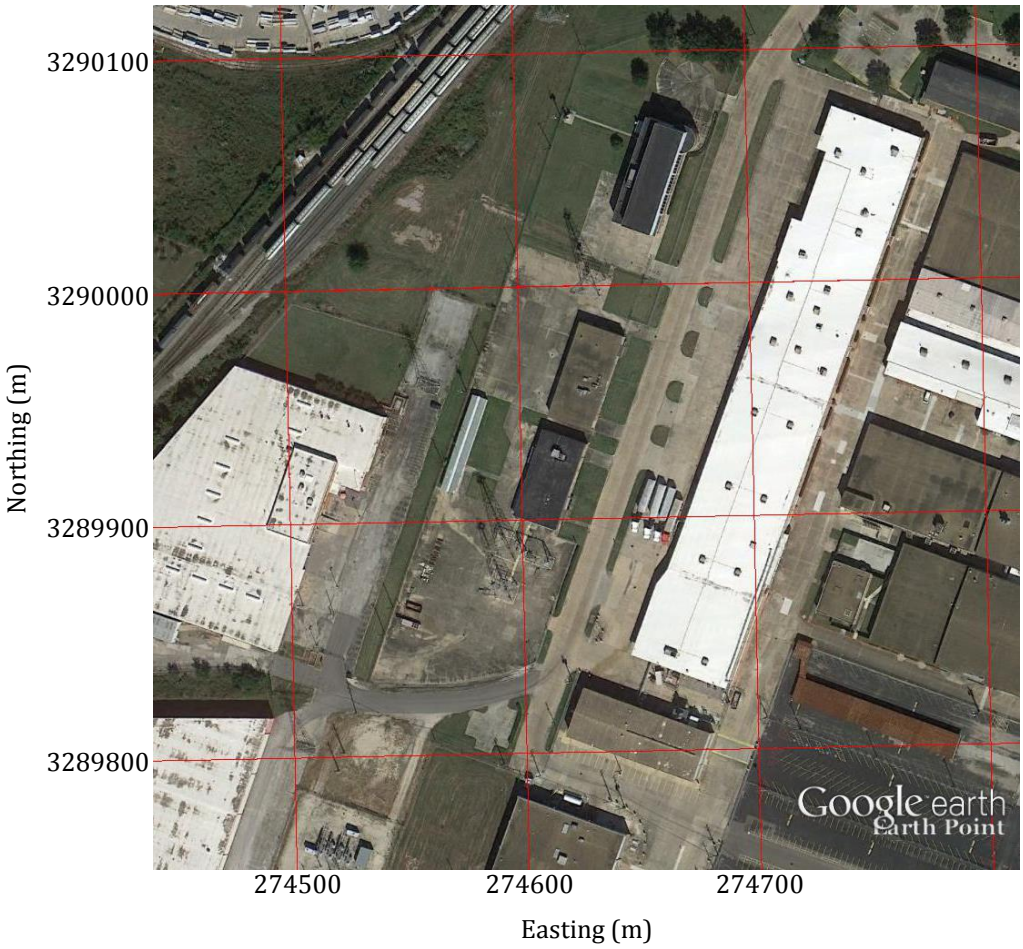

Figure 16: Survey location at Energy Research Park, University of Houston

3.1 Control Data

The TLS control data was collected at the project site using the RIEGL VZ-400 in static mode. Four stationary scan positions were used to fully cover the survey area, maximize point

density, and minimize occlusions. Retro-reflective targets were placed throughout the project area to act as known points within each scan position (see Figure 17). These targets were utilized to register the separate scan positions together, as well as to provide global coordinates for the pointcloud. With the VZ-400 and RIEGL's proprietary software, the targets were fine-scanned at high density to function as scan position tiepoints. The properties of the retro-reflective targets were designated in the software so a model could be defined and the coordinates at the center of the tiepoints calculated.

Figure 17: Retro-reflective target used as TLS tiepoint

To acquire global coordinates, a GNSS network was established as control for the TLS data collection. One GNSS "base station" was set up and collected data during the entire extent of the survey time. A second receiver was used to measure the positions of multiple control points, corresponding to the retro-reflective targets, during the TLS data collection. Observations were taken at each tiepoint for 20-30 min.

3.2 Test Data

3.2.1 Mapping-Grade MLS Data Collection

The operation of the backpack MLS was relatively simple. First, the GNSS receiver was initiated. Manufacturer software was required to configure and log the data. When satellite lock was detected, the receiver was started; it recorded data at a 2-Hz rate. This data was sent to the IMU via an RS-232 serial cable to provide high-accuracy positioning. Only binary OEM-V format logs could be used with the NovAtel receiver.

Next, the IMU was started. Using proprietary INS acquisition software, the collection configurations of the Inertial+2 could be set to the desired values. The instrument was also prepared to receive the OEM-V binary format messages from the GNSS receiver for position. Antenna splitters allowed the GNSS signal to assist in heading determination. Because of the dual antennas and heading assistance, the Inertial+2 is able to initialize in static mode. The instrument logged the data it collected internally, and the raw observations were recorded at 100 Hz.

Last, the Velodyne LiDAR instrument was begun. A custom-programed UDP packet logger was utilized. This recorded, among other variables, time-stamped range and angle measurements from the laser scanner.

A total of four datasets, over the two days, were collected with the mapping-grade system in backpack mode. The platform was walked around the project site at 3-5 $^{km}/_{h}$ for intervals of approximately 15-20 min. The orientation of the laser scanner was also adjusted between datasets. An approximate zenith angle of 10° was applied to Dataset 1 and 3, and an approximate angle of 50° for Dataset 2 and 4 (see Figure 18). This caused the instrument to be “aimed” toward the ground for Dataset 2 and 4, resulting in smaller swath widths and shorter average ranges.

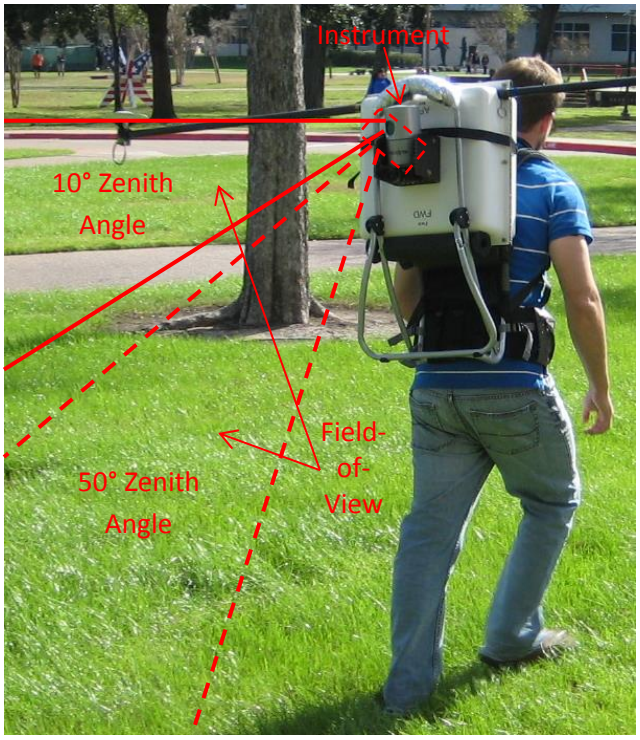

Figure 18: Adjustable orientation of laser scanner on backpack

The project area was covered by adjacent flightlines to assure that objects were surveyed from more than one pass, and in multiple directions, from a variety of ranges. Some cross flightlines were also traversed to assure that objects were completely observed. The rotating scanner head was ideal for extensive data collection, because it limited occlusions. A standalone GNSS receiver and antenna was also operated simultaneously to provide a reference position for the kinematic system during post-processing.

3.2.2 Survey-Grade MLS Data Collection

A cart was used for mobilization of the survey-grade MLS system. The cart was pushed around the project area at similar speeds as the backpack collection. Approximately 30 min of data was recorded. A static GNSS base station was operated concurrently, as before, for an overlapping 2-h period.

First, the LANDINS was started. This commenced the GNSS receiver and IMU operation. When GNSS position was determined, the GNSS and raw IMU data recording was activated through a manufacturer's user interface. The data was stored internally to the instrument. The GNSS took measurements at 1 Hz and the IMU at 100 Hz.

Next, scanning by the VZ-400 began. The instrument was operated in single line mode. In this mode, the horizontal rotation and horizontal encoder of the scanner is locked. A custom script was utilized to set the needed instrument variables and record data. The scanner also contains an internal L1 GNSS receiver. This was used to time-stamp the raw data for later georeferencing.

Multiple flightlines were again made throughout the project site in adjacent and cross passes. Because the instrument scanned with a single vertical line pattern, careful attention was made to fully cover objects of interest. For instance, in this case it is easy to exclude planar surfaces that are perpendicular to the flightline, because the laser beam is also perpendicular to the direction of travel. This is opposed to the rotating scanner, which can observe an object from multiple look-directions along a flightline.

4 PROCESSING

Processing procedures for kinematic LiDAR are important because simple mistakes can be made that adversely affect the outcome of the resulting pointclouds. Several processing blunders, such as incorrect kinematic antenna height, atmospheric modeling, processing profiles, and *z* lever-arm estimation, were discovered during the analysis, which had to be corrected. Additionally, care must be taken to make realistic assumptions of instrument errors used in the Kalman filters, or the reported post-processed estimates will be overly optimistic. The following sections give an overview of the post-processing applied to both the TLS and MLS datasets.

4.1 Control Data Processing

4.1.1 GNSS

A GNSS base station was used as control for the GNSS network. The raw data was uploaded to the National Geodetic Survey's On-line Positioning User Service (OPUS). This service determines the mean of three single-baseline solutions to provide its reported position. A more in-depth look at the method and accuracy of this service can be found in Soler et al. (2005).

The results from OPUS offered an overall RMS (root-mean-square) of ± 1.6 cm. This statistic was acceptable, as it should be less than ± 3.0 cm (Snay et al. 2011). The estimated standard deviations in latitude, longitude, and height were ± 0.3, ± 2.2, and ± 5.3 cm, respectively. Therefore, the point was held as control. Using static GNSS processing software, the full network was processed with a precise ephemeris file to determine the baselines between stations. Finally, a least-squares adjustment was applied to the post-processed GNSS observations, resulting in relative accuracy levels of under ± 2 cm horizontal (see Table 6).

Table 6: Standard deviations from GNSS network after least-squares adjustment

Station	Standard Deviation Horizontal (m)	Standard Deviation Vertical (m)
Base	0.014	0.05
1	0.016	0.05
2	0.016	0.05
3	0.016	0.05
4	0.016	0.05

4.1.2 TLS

Each tiepoint required for registering the scan positions together was located in the SOCS at each specific scan position. Using the geometry of the tiepoints, RIEGL's RiSCAN PRO software was utilized to register the scan positions together into a project coordinate system. The project coordinate system was then related to the global coordinate system through the GNSS measurements of selected retro-reflector tiepoints, as discussed in Section 4.1.1. Finally, a least-squares adjustment was performed on the registered scan positions to assure the highest quality data possible. Planar patches were created from the collected data at each position, within the software, so an iterative closest point procedure could be used to precisely align the individual laser scans (RIEGL 2011). The TLS data was ideal for this operation, as multiple horizontal and vertical planes were present in the data. The best-fit estimation resulted in a highly precise pointcloud. Table 7 shows the residual differences between the separate scan positions.

Table 7: Differences between positions from TLS data after least-squares adjustment

	Scan Position 1	Scan Position 2	Scan Position 3 (Locked)	Scan Position 4
ΔX (mm)	3	1	0	−2
ΔY (mm)	3	1	0	2
ΔZ (mm)	3	1	0	1
Δω (°)	0.000	0.000	0.000	−0.002
Δϕ (°)	0.002	0.001	0.000	0.000
Δκ (°)	0.002	0.000	0.000	−0.003
ΔS (mm)	0	0	0	0

The standard deviation of the distances between planar pairs of different scan positions in the final adjustment was ± 3.9 mm. The residuals from the point distances were normally distributed and most were sub-centimeter (see Figure 19). Overall, the TLS control data can be considered highly accurate.

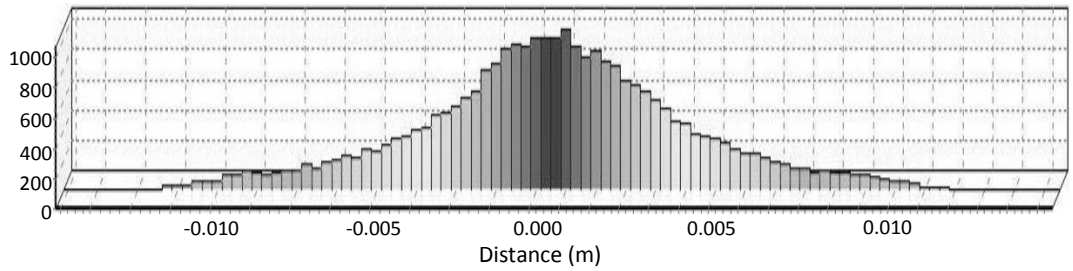

Figure 19: Point distance residuals from TLS data after least-squares adjustment

4.2 Trajectory Estimation

4.2.1 Mapping-Grade System Trajectory

The first step in post-processing the Inertial+2 INS data was processing the GNSS records. The 1.3-h static observation data, from Section 3.2.1, was sent to OPUS-RS (Rapid Static). This is similar to the OPUS processing discussed in Section 4.1.1, but designed for rapid static datasets less than 2 h long. The position results of the OPUS-RS processing had unitless normal-

ized RMS values of 0.338 and 0.355 for the two days, respectively. These were acceptable designations, as they should be less than 1. Also, all the quality indicator numbers were over 3, which is suggested (see Schwarz et al. (2009) and Snay et al. (2011) for more details). The estimated accuracy in position is reported in Table 8. The method for OPUS-RS is slightly different from OPUS because of shorter observation times, and the results can often have less accuracy than observation times over 2-3 h. However, the results obtained here were at optimal levels. Separate control was used for the different TLS and MLS datasets, because the surveys were performed at different times.

Table 8: Estimated accuracy in position from OPUS-RS

(cm)	Day 1	Day 2
Latitude	0.8	0.6
Longitude	0.4	0.5
Height	5.3	1.8

Waypoint GrafNav was utilized to solve static-to-kinematic baselines for a final backpack system trajectory. A raw GNSS file was extracted from the raw navigation files. This file was the mobile GNSS data that the NovAtel receiver sent to the Inertial+2. First, the file was converted into Waypoint's raw GNSS receiver independent format. Next, the static base station data and control coordinates were added for differential GNSS processing.

Then, the kinematic data was processed. Differential GNSS processing was completed in both forward and backward directions. Dual-frequency observations were used, along with a 12.5-15.0° elevation mask, to reduce atmospheric and multipath effects. The forward and backward trajectories were optimally combined, using the Kalman filter concept introduced in Section 1.2.2, and the data was exported in an OxTS software-recognizable file format, at 1 Hz.

These procedures were done for all four datasets. The estimated positional standard deviations for the four datasets are compiled in Table 9.

Table 9: Standard deviation percentages from post-processed, kinematic GNSS solutions

	Observations (%)			
Standard Deviation (m)	**Dataset 1**	**Dataset 2**	**Dataset 3**	**Dataset 4**
0.00 - 0.10	96.2	97.0	96.2	96.3
0.10 - 0.30	1.3	0.0	3.2	1.4
0.30 - 1.00	0.0	0.0	0.0	0.4
1.00 - 5.00	2.6	1.0	0.2	0.3
5.00 +	0.0	2.0	0.4	1.6

To understand the quality of the data from the KF better, the forward-and-backward separations were reviewed. Since these represent two independent solutions, the separation is a good indicator of the noise level of the data. The RMS of the differences at each epoch between the forward-and-backward solutions is given in Table 10.

Table 10: RMS of forward-and-backward separation in position

(m)	**Dataset 1**	**Dataset 2**	**Dataset 3**	**Dataset 4**
Latitude	0.111	0.237	0.337	0.223
Longitude	0.168	0.082	0.751	0.502
Height	0.102	0.472	0.964	0.803

These values were much poorer than expected. In two particular regions of the survey area, multipath or GNSS outages were regularly experienced due to blockages from buildings. These parts of the trajectory suffered from a low number of satellites and poor PDOP (Positional Dilution Of Precision). This significantly affected the GNSS trajectory accuracies. Figure 20 shows the areas of interest for the trajectory of Dataset 1. It can be seen that the forward-and-backward separation increased considerably at these locations, which affected the RMS values

given in Table 10. Apart from these areas, the separation is small, indicating a good KF solution. Table 11 shows the improvement in the RMS of forward-and-backward separation when the areas of poor GNSS are removed. Fortunately, the INS Kalman filter can easily bridge any data gaps, although its accuracy can still suffer.

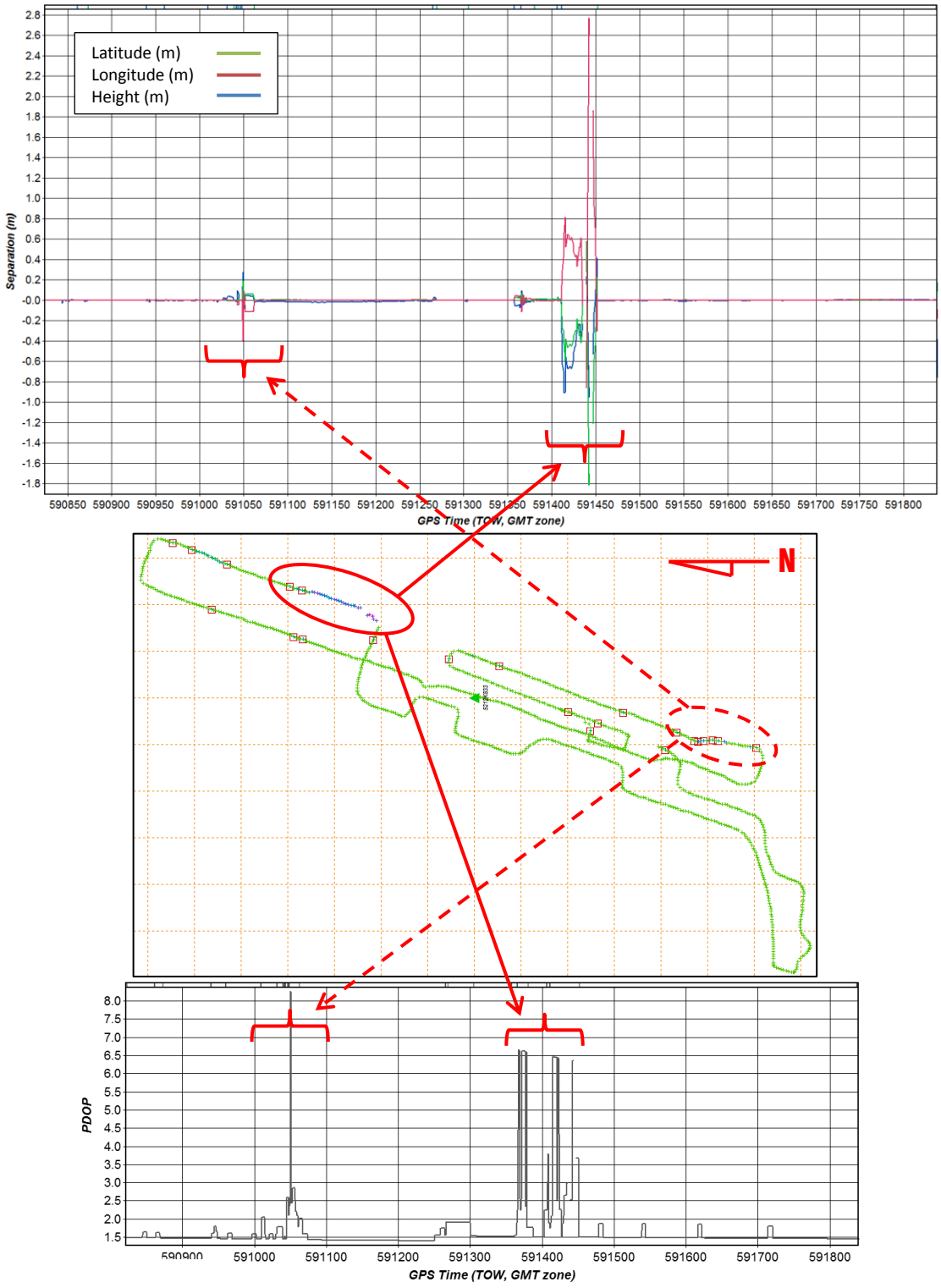

Figure 20: Separation (top), trajectory (middle), and GNSS PDOP values (bottom) for Dataset 1

Table 11: RMS of separation in position with poor GNSS areas removed

(m)	Dataset 1	Dataset 2	Dataset 3	Dataset 4
Latitude	0.007	0.032	0.028	0.092
Longitude	0.008	0.010	0.097	0.102
Height	0.027	0.099	0.308	0.095

The second procedural step was processing the inertial data with RT Post-Process. The raw IMU observation file was extracted from the instrument and converted to its software-usable data format. An instrument configuration file was also extracted. This file was reviewed to assure that the roll, pitch, and heading (ω, φ, κ) orientation parameters of the instrument with respect to the body frame were correct. In addition, the INS measurement origin to the GNSS antenna phase center (x, y, z), and the separation, orientation, and height (d, o, h) between the primary GNSS antenna and the secondary antenna were included, after being estimated from physical measurements and engineering drawings. Reasonable estimated errors were entered using OxTS i+config software for use in the KF (see Table 12).

Table 12: Position and orientation parameters for GNSS and INS instruments

Parameter	Measurement	Standard Deviation
ω (°)	0	5
φ (°)	-90	5
κ (°)	90	5
x (m)	0.015	0.020
y (m)	-0.869	0.010
z (m)	-0.343	0.020
d (m)	1.922	-
o (°)	90	5
h (m)	0.000	0.020

Then, the pre-processed data file was selected, and the processing started. The data was integrated with the final GNSS trajectory, in forward and backward directions, and combined. The final position and orientation was output for a selected period at 100 Hz in a *.pos* format, using time in UTC (Coordinated Universal Time).

The Kalman filter estimated the standard deviations of attitude and position; these are shown in Figure 21. As can be seen, the position accuracy suffers for an approximately 40-s period. This corresponds to the findings in Figure 20, where the GNSS experienced poor performance from signal blockage. This also affected the heading accuracy, which relies heavily on the GNSS signals to determine its orientation with respect to north. The heading accuracy also deteriorated significantly in other areas where GNSS coverage was only briefly degraded. Here the other estimated orientation parameters did not suffer. This shows the importance of good GNSS coverage throughout a survey. In the future, the trajectory could be improved by more precautious GNSS/INS collection techniques, such as maximizing obstruction avoidance where possible. However, in areas with good GNSS, the INS very performed well.

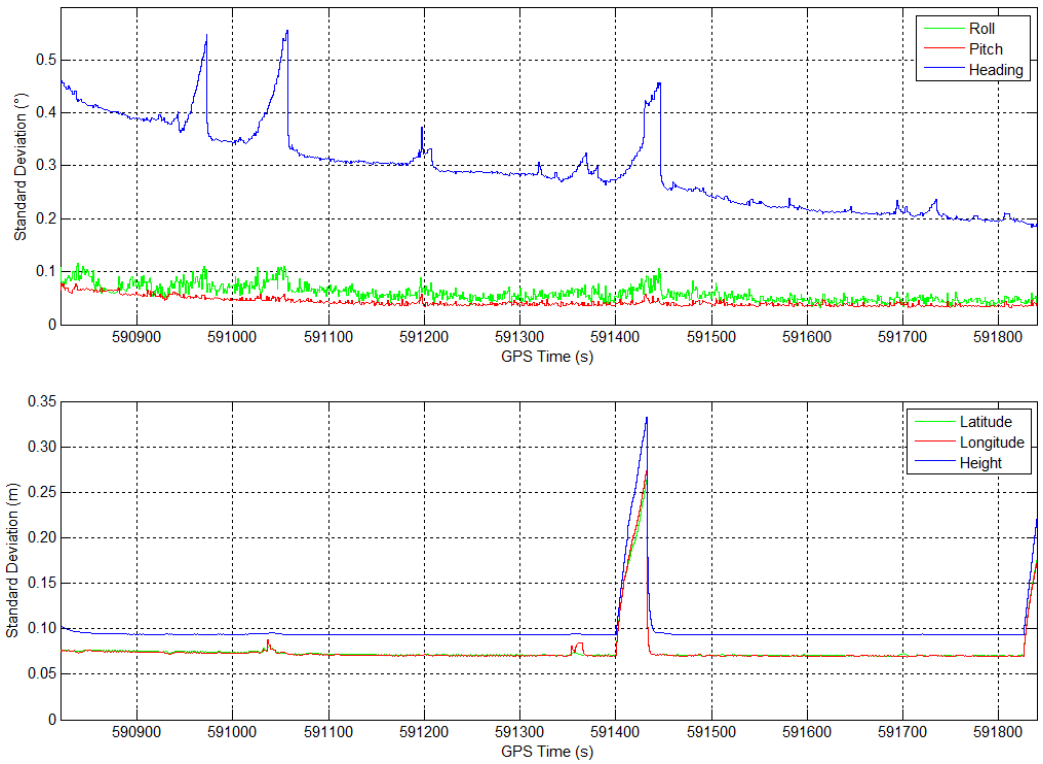

Figure 21: Standard deviations in attitude (top) and position (bottom) estimated by filter

The GNSS/INS integration approach, as seen, was a loosely-coupled method. Using this methodology, a GNSS-only filter is first implemented separately, followed by the GNSS/INS integration. This utilizes the final position and velocity of the GNSS trajectory as updates to the INS filter. This is opposed to a tightly-coupled integration technique, which processes the GNSS and IMU measurements together (see Figure 22). Although the performance of a loosely-coupled approach is not as accurate or rigorous as tightly-coupled integration, it is more versatile and straightforward (Groves 2008). For simplicity, it was the technique implemented in the research.

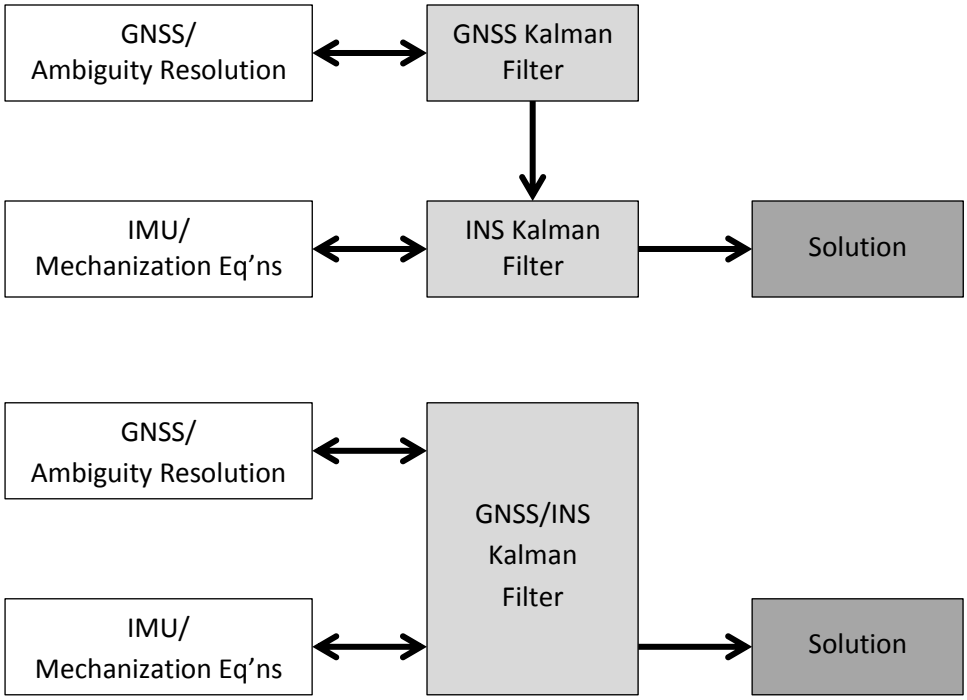

Figure 22: Loosely-coupled (top) and tightly-coupled (bottom) GNSS/INS integration

4.2.2 Survey-Grade System Trajectory

With the survey-grade system, the first step to processing the trajectory and LiDAR data was to process the GNSS data. To avoid repetition, the same procedure as given for the mapping-grade MLS system was completed for the static and kinematic processing of the survey-grade system. The only differences were the use of OPUS for the 2-h static data, and a different raw kinematic GNSS format, which was again converted to Waypoint's proprietary format. The OPUS results for the static base station had an overall RMS of ± 1.9 cm. Meanwhile, the distribution of standard deviations in position and RMS of the separation in forward-and-backward solutions were significantly improved over the mapping-grade trajectory (see Table 13).

Table 13: Statistics from post-processed, kinematic GNSS solution

Standard Deviation (m)	Observations (%)	Position (m)	Forward-and-Backward RMS Separation (m)
0.00 - 0.10	99.7	**Latitude**	0.020
0.10 - 0.30	0.3	**Longitude**	0.007
0.30 +	0.0	**Height**	0.046

Figure 23 shows that the forward-and-backward separation had large discrepancies in two places. This corresponded to locations with poor PDOP. Unlike the mapping-grade system trajectory, the large separations were not sustained for any amount of time. This was due to better care being taken in avoiding obstacles that would negatively affect the GNSS signals and therefore the trajectory.

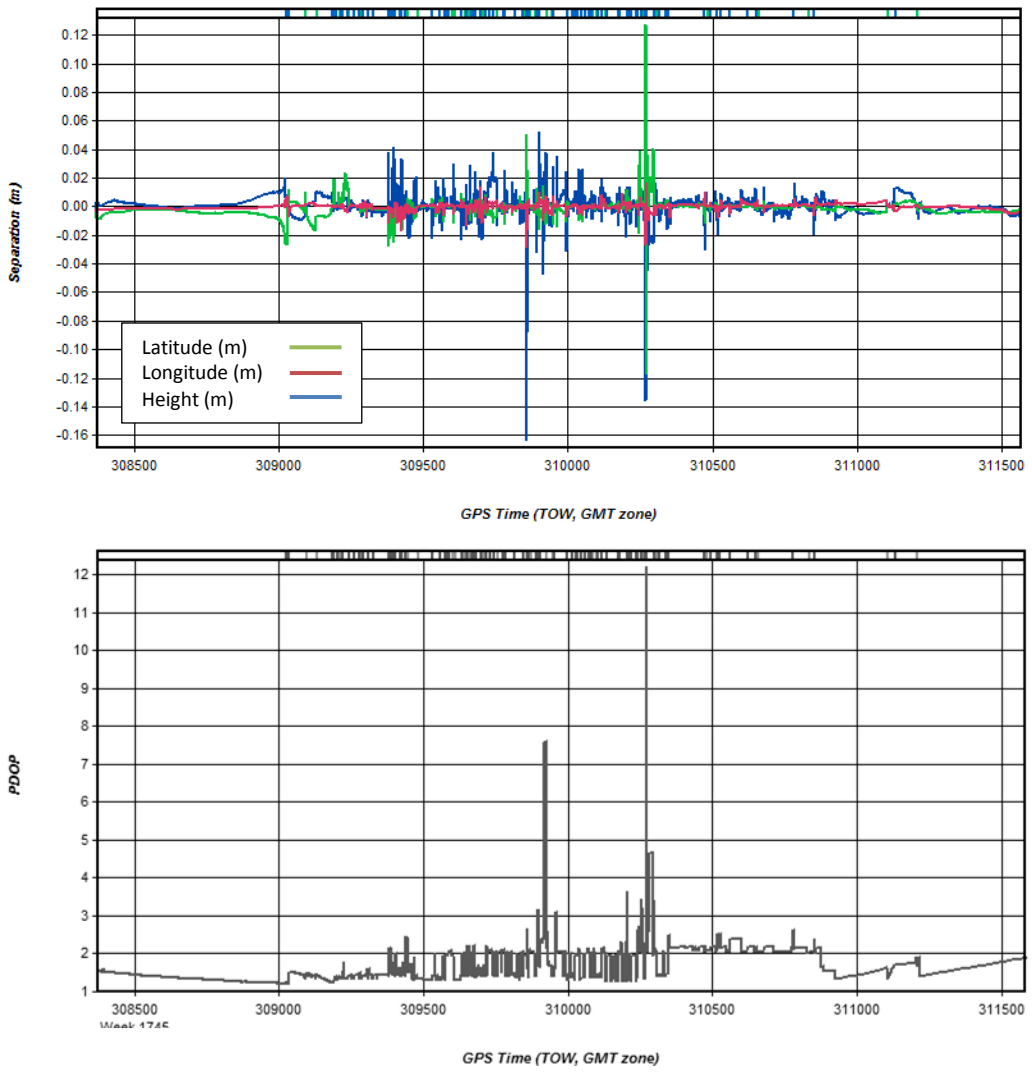

Figure 23: Trajectory separation (top) and GNSS PDOP values (bottom)

The GNSS/INS data was post-processed using DELPH INS, software created for iXSea products. Like RT Post-Process, this was a loosely-coupled integration approach. The newly processed kinematic GNSS solution was imported, and the lever-arm between the INS measurement center and antenna phase center was determined from engineering drawings (see Table 14).

Table 14: Position and orientation offsets between GNSS and INS instruments

ω (°)	0
φ (°)	0
κ (°)	0
x (m)	0
y (m)	0
z (m)	0.520

Then, the integrated KF procedure was implemented in forward and backward directions. These calculations were combined using the previously discussed smoothing technique and exported in SBET (Smoothed Best Estimate of Trajectory) format at 100 Hz. The estimated accuracies of the final trajectory can be seen in Figure 24. The overall performance of this instrument was excellent. The higher accuracy of the LANDINS IMU allowed it to bridge the GNSS data gaps without significant degradation in accuracy.

Figure 24: Standard deviations in attitude and position estimated by DELPH INS KF

4.3 Scanner/Trajectory Integration

4.3.1 Mapping-Grade System Integration

4.3.1.1 Laser Calibration

As stated in Section 2.1.1, the Velodyne HDL-32E requires internal calibration parameters. These values are supplied by the manufacturer. Previously, it had been discovered that a rigorous static calibration, using planes, could be applied to significantly improve a Velodyne scanner's calibration (Glennie and Lichti 2010). In this method, the LiDAR points are constrained

to lie on planes, and therefore the points can be used to estimate the planar variables, along with the instrument calibration parameters, through a least-squares solution.

Static data was collected with the HDL-32E in an environment of strictly planar surfaces. Collection was performed with the instrument in multiple horizontal and vertical angles, and from two locations, to optimize the calibration's ability to account for systematic errors. The correction procedure was performed, and misclosure vectors with respect to planar surfaces in the pointclouds were calculated for 100,000 data points. These vectors were computed for pointclouds both before and after the calibration. A 20% improvement in the instrument accuracy was determined (Glennie et al. 2013). These calibration parameters were subsequently used for all work with this particular Velodyne instrument.

4.3.1.2 Boresight Calibration

The boresight and lever-arm calibration parameters were calculated using a custom algorithm. This process was based on the planar approach used in Glennie (2012). First, the boresight and horizontal lever-arm values were estimated, and geo-referencing was performed with these values, using a method to be presented in Section 4.3.1.3.

From the resulting pointcloud, 40 planar surfaces were manually selected. The planes were in different orientations: horizontal, vertical, and sloped. The software accepts a calibration file, an "extended information" file from the geo-referencing procedure, and the selected planes from the pointcloud. The calibration file contains the boresight angles and lever-arm offsets between the INS and scanner, as well as the correction factors specific to the instrument, per Section 4.3.1.1. Finally, the output gave estimated boresight and lever-arm parameters and accompanying quality information. This process was repeated two to three times for each dataset, with the updated parameters successively used, to ensure the best results.

Figure 25 shows a section view of a garage door and driveway. The green points show the pointcloud before boresight and lever-arm calibration, and the magenta points show the pointcloud after calibration. As can be seen, a significant improvement was made using the calibration, especially on the horizontal plane.

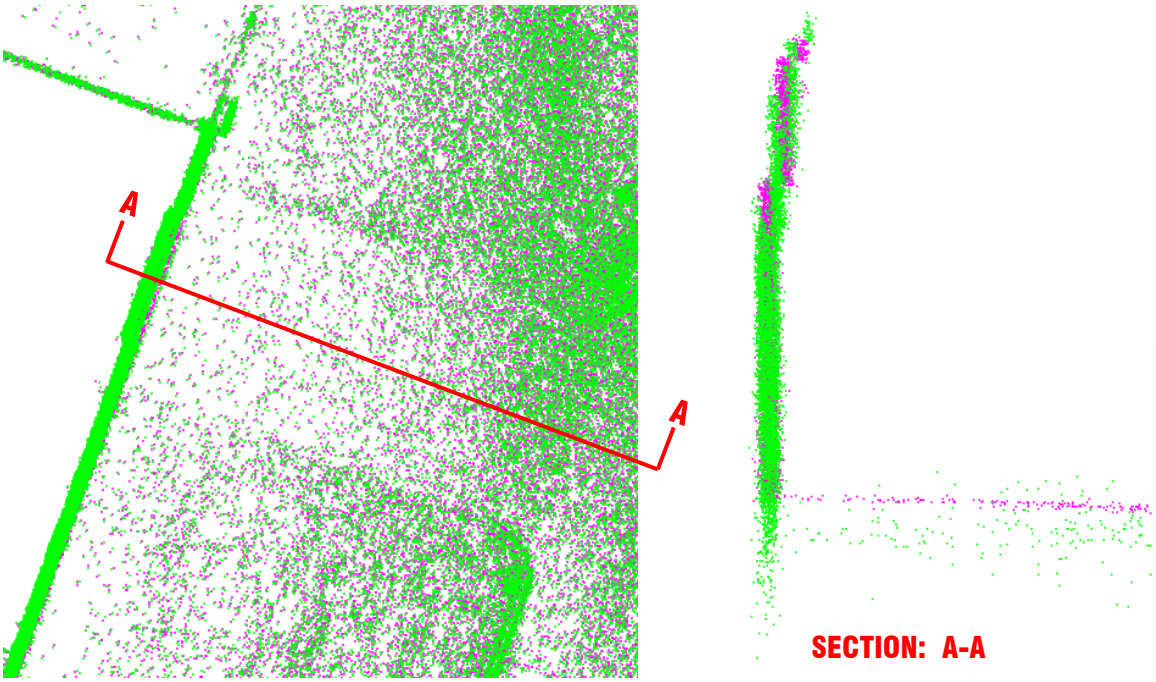

Figure 25: Pointcloud section before and after boresight and lever-arm calibration

The orientation parameter standard deviations and planar misclosure statistics of the calibration datasets are given in Table 15. As was shown in Table 10, Dataset 3 had Kalman filter separation values much larger than the other sets. This pointcloud was deemed unusable for further accuracy analysis, because too many errors were present in the data, which would negatively influence an accuracy study. In addition, it appeared visually inadequate by simple qualitative observation. This was due to the poor GNSS positioning in certain areas of the data from loss of lock, etc. The INS could not resolve the large data gaps present in the GNSS positioning well enough, and it is therefore neglected here and throughout the rest of the analysis. It should also be noted that the *z* lever-arm is not present in Table 15. As reported in Glennie (2012), this

parameter is too weakly observable to estimate because of lack of variation in planar patch orientation, and was thus given by manual adjustment.

Table 15: Statistics from boresight and lever-arm calibration

		Dataset 1	Dataset 2	Dataset 3	Dataset 4
Estimated Standard Deviations of Orientation	**Roll (°)**	0.0050	0.0190	–	0.0163
	Pitch (°)	0.0040	0.0060	–	0.0034
	Heading (°)	0.0020	0.0044	–	0.0038
	***X* Lever-Arm (m)**	0.0004	0.0008	–	0.0038
	***Y* Lever-Arm (m)**	0.0013	0.0018	–	0.0004
Planar Misclosure After Adjustment	**Minimum (m)**	−0.1912	−0.1898	–	−0.1778
	Maximum (m)	0.2018	0.1883	–	0.1773
	Mean (m)	0.0000	0.0000	–	0.0000
	RMSE (m)	0.0404	0.0385	–	0.0365

To fully demonstrate the improvement from the calibration, the planar residual distribution before and after the procedure was plotted. Figure 26 shows the residuals of points to the 40 planes, for Dataset 1, before the final iteration of the calibration and after the final iteration. A significant improvement was made, resulting in residuals normally distributed about the mean. The standard deviation of the residuals improved from ± 0.245 m to ± 0.043 m.

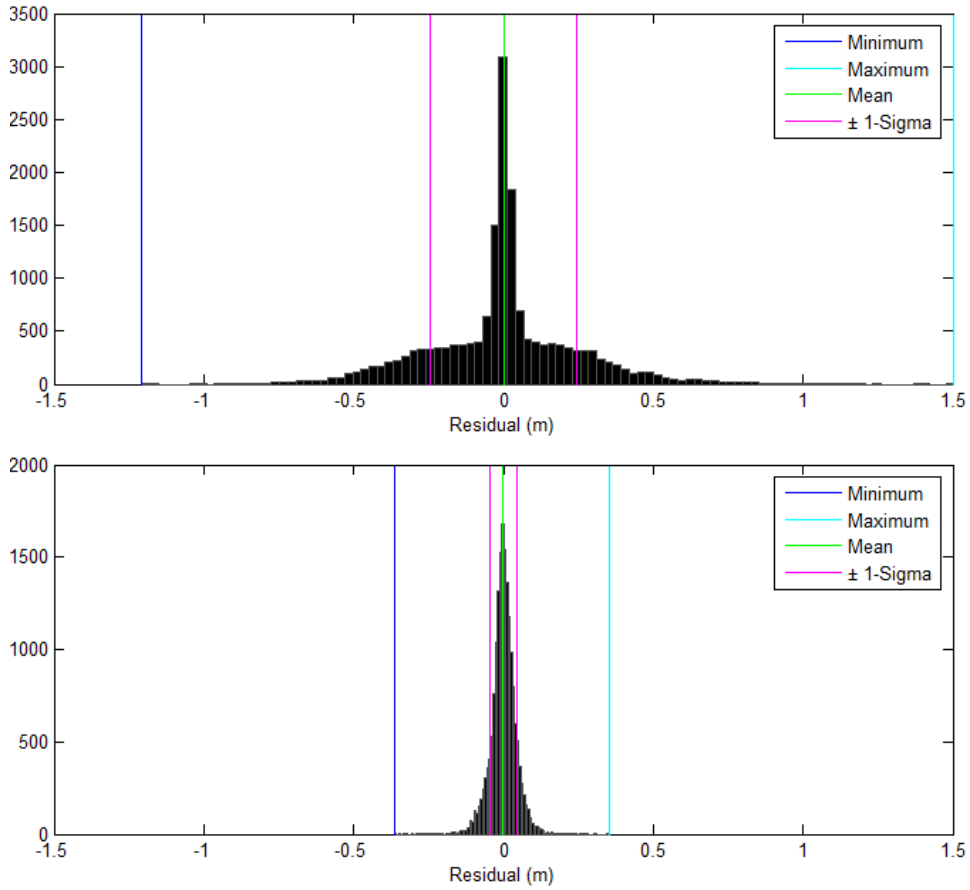

Figure 26: Residuals of planar points before (top) and after (bottom) calibration

4.3.1.3 Geo-Referencing

For final data integration, a second custom-developed software package was utilized. The software used Velodyne laser Equation 3 and geo-referencing Equation 2 to rotate and translate the LiDAR points from the s-frame to the l-frame, determining the final geo-referenced pointcloud as described in Section 1.2.3. This software accepts the raw Velodyne output file, the *.pos* file from the processed GNSS/INS trajectory procedure, and the aforementioned calibration file. The output is a final geo-referenced pointcloud (see Figure 27).

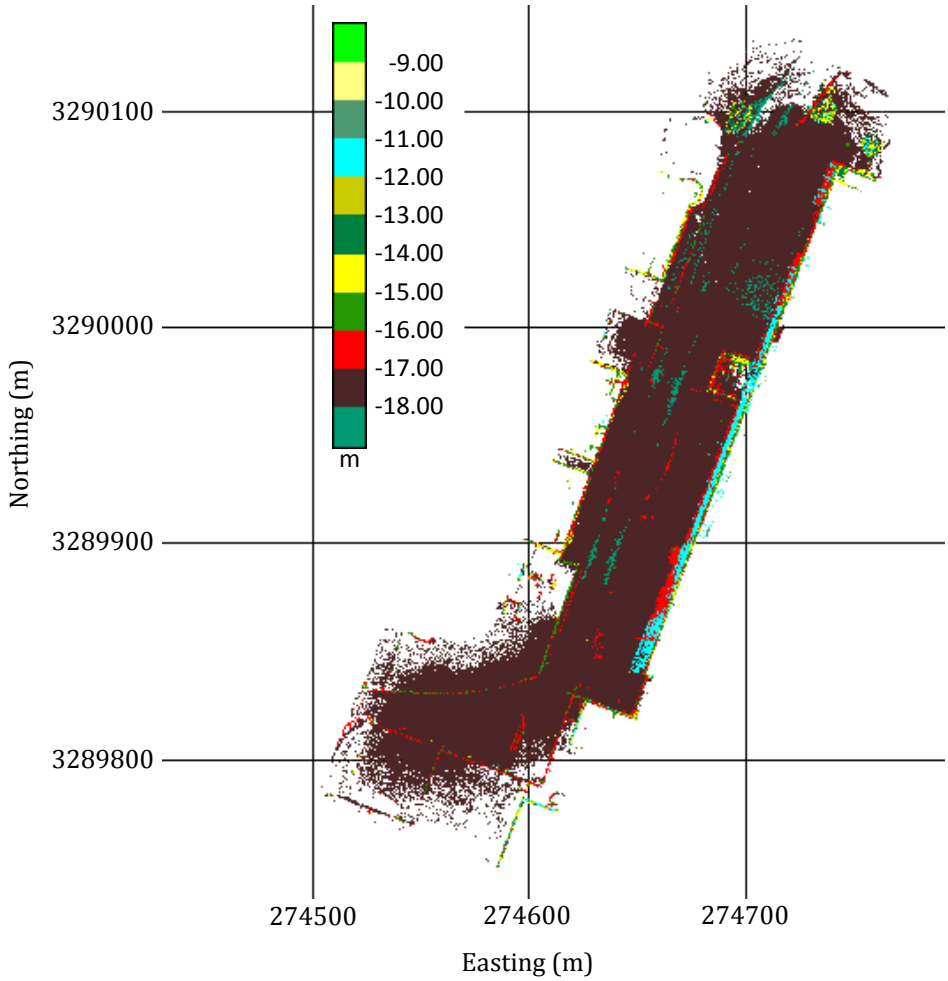

Figure 27: Final geo-referenced pointcloud of project area (Colored by ellipsoid height)

A final interesting statistic from the post-processing is the number of returns calculated by the software (see Table 16). The data was filtered with a decimation rate of 25, so it would be computationally efficient. Nevertheless, it can be seen that the pointclouds still contain large numbers of returns. Even more remarkable are the number of pulses sent out by the instrument that do not register a return. The number of valid returns computed was less than 1% of what is possible. This number can be improved by reducing or disregarding the decimation rate and determining the optimum instrument orientation to maximize returns. This shows the ability of the Velodyne HDL-32E to collect dense information.

Table 16: Laser scanner pulses versus returns

(Decimation Rate = 25)	Number of Pulses	Number of Returns Output	% Returns
Dataset 1	708,251,904	6,079,251	0.86
Dataset 2	624,807,168	3,499,385	0.56
Dataset 4	957,535,488	5,914,787	0.62

4.3.2 Survey-Grade System Integration

The same approaches for boresight calibration and geo-referencing were performed for the survey-grade system. The least-squares planar adjustment for determining the boresight angles was computed using the same custom-developed software. The resulting calibration gave statistics that demonstrated the system's efficient collection ability (see Table 17). All of the results, with the exception of the heading, are substantially better than the calibration from the mapping-grade MLS system. Most notably, the RMSE of the residuals on the planar surfaces after calibration is nearly four times better.

Table 17: Statistics from boresight calibration

Estimated Standard Deviations of Orientation (°)	**Roll**	0.0011
	Pitch	0.0016
	Heading	0.0034
Planar Misclosure After Adjustment (m)	**Minimum**	−0.0485
	Maximum	0.0486
	Mean	0.0000
	RMSE	0.0097

Equation 2 was applied to rotate and translate the LiDAR points into a geo-referenced pointcloud. First, the raw scanner observations were converted into a usable binary format. Then, the observations, SBET file, and a boresight and lever-arm calibration file were integrated to deliver a final output pointcloud. Additional accuracy assessment of the survey-grade point-cloud is reported in Section 5.2.

5 RESULTS & ANALYSIS

As stated in the research objectives, the analysis was focused on evaluating the accuracy of the mapping-grade MLS system, which is not well understood. The geo-referenced datasets processed in Section 4 were compared to pointclouds from a high-accuracy TLS instrument and a survey-grade MLS system. The final results were also compared to the expected system accuracy.

5.1 Mapping-Grade MLS v. TLS

5.1.1 Data Overview

The size of the encompassed survey area was 15,000-20,000 m^2. The system recorded data at an elevation of up to 20-25 m, with most usable data less than 15 m above ground level. Again, only Datasets 1, 2, and 4 are being analyzed.

From an observational standpoint, Dataset 1 is the best pointcloud overall. Because of the near vertical laser scanner orientation, it had the most complete coverage of the surrounding areas, providing point densities from hundreds to thousands of points per square meter. Datasets 2 and 4 had less coverage, because a significant portion of the field-of-view was aimed toward the ground. Some areas lacked LiDAR returns because of this orientation (see Figure 28).

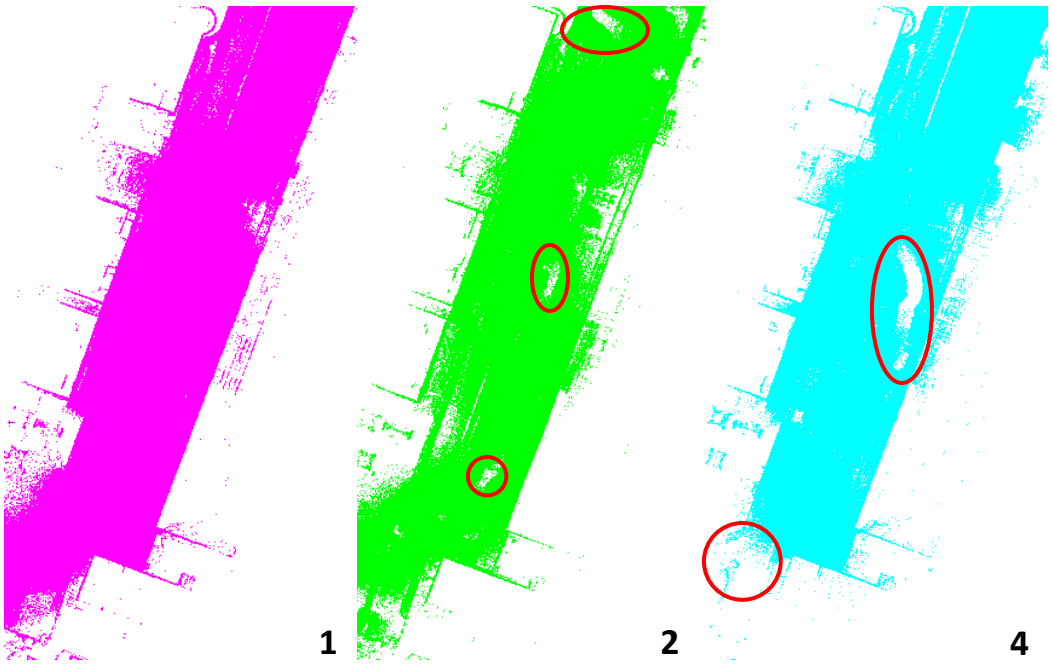

Figure 28: Pointcloud coverage of survey area
(Significant data occlusions highlighted with red ovals)

In addition, Dataset 1 is the cleanest in some of the GNSS-sensitive areas of the survey location. Some noise and data shifts occurred next to specific buildings in the project area where the GNSS had trouble maintaining good position (see Section 4.2.1 for discussion). When considering the absolute accuracy of the system in ideal conditions, these small regions can be ignored in favor of quality areas. Nevertheless, they must be noted as a consideration for overall operational capability.

5.1.2 Pointcloud Results

Several approaches were taken to analyze the horizontal and vertical accuracy of each MLS pointcloud. First, three methods of planar analysis were performed to estimate the general accuracy of the pointclouds. Then, using the planar data, a comparison of the MLS results to the expected accuracy of the system was done to investigate if the observed level of performance

was as expected. Finally, analysis of different approaches to feature and extraction analysis were completed to evaluate the accuracy for data modeling applications.

5.1.2.1 Pointcloud Comparison

A point-to-plane comparison was the main assessment method used. Twenty-five planar sections were selected from each dataset, for a total of 75 planes. Corresponding planar features from the TLS data, to be used as control, were also selected. The planar patches had dimensions of 1-2 m, with the largest being ~3 m, to minimize any surface variations and ensure actual planar sections were used. Each plane contained hundreds to thousands of points because of the density of the data; some of the TLS data planes consisted of tens of thousands of points. A least-squares fit was applied to each set of points to determine the best-fit plane equation of each planar patch. A singular value decomposition (SVD) method was utilized (Shakarji 1998). These equations were used throughout the analysis. Then, point-to-plane distances were calculated for both the TLS and MLS planes and were considered the residuals of the pointcloud points from their true location.

The statistics for the residuals of the TLS patches were recorded to confirm that good data was being used for comparison (i.e., the surface was actually planar). The statistics for the MLS planes were noted to ensure a realistic comparison could be made. If the plane appeared exceptionally bad, it was rejected. Additionally, the angle between the estimated planes was calculated as a check. For instance, if a small area was selected and significant noise was present, the SVD method could estimate the plane as being in the direction of the noise rather than the true surface direction; the angle between planes could identify this issue.

Finally, the distances from the MLS planar points to the TLS control plane were determined. This was the estimation of the deviation of the MLS points from the assumed truth. This

is sensibly the most pure approach of comparison. Table 18 presents typical results of this procedure for a single plane in Dataset 1.

Table 18: Typical results of plane comparison between MLS and TLS data

(m)	TLS Residuals	MLS Residuals	MLS v. TLS Plane
Minimum	-0.0093	-0.1073	-0.0663
Maximum	0.0195	0.1165	0.1628
Unsigned Mean	0.0027	0.0386	0.0495
Mean	-0.0000	-0.0000	0.0382
Standard Deviation	0.0033	0.0453	0.0453
RMS	0.0033	0.0452	0.0592

Overall, the results were encouraging. A majority of the mean differences of the MLS points to 75 TLS planes were from 1-7 cm. The mean of the TLS residuals were all essentially zero (using signed residuals), with most having standard deviations of ± 5 mm or less. This was around the stated accuracy of ± 5 mm of the VZ-400 laser scanner. This also shows that the TLS data was an excellent tool for comparison.

Next, a plane-to-plane comparison was completed. This was done by using the best-fit planes of the point selections. The centroid of the MLS data was determined, and the distance to the TLS control plane, along the normal of the estimated MLS plane, was calculated. This technique compared the typical location of the MLS plane, as opposed to the individual points, with the truth. Nominally, this calculation agreed with the mean values from the point-to-plane evaluation.

Finally, a point-to-point analysis was conducted. Using the planar patches, the distances from each MLS point were calculated to the nearest neighboring TLS point. This method was conducted to investigate the distance between the pointcloud patches separately from the planes. An open-source software, CloudCompare, was employed to calculate the distances and

statistics of the point-to-point comparisons. For the most part, the trends of the residuals were similar to those reported above. Figure 29 shows a typical result.

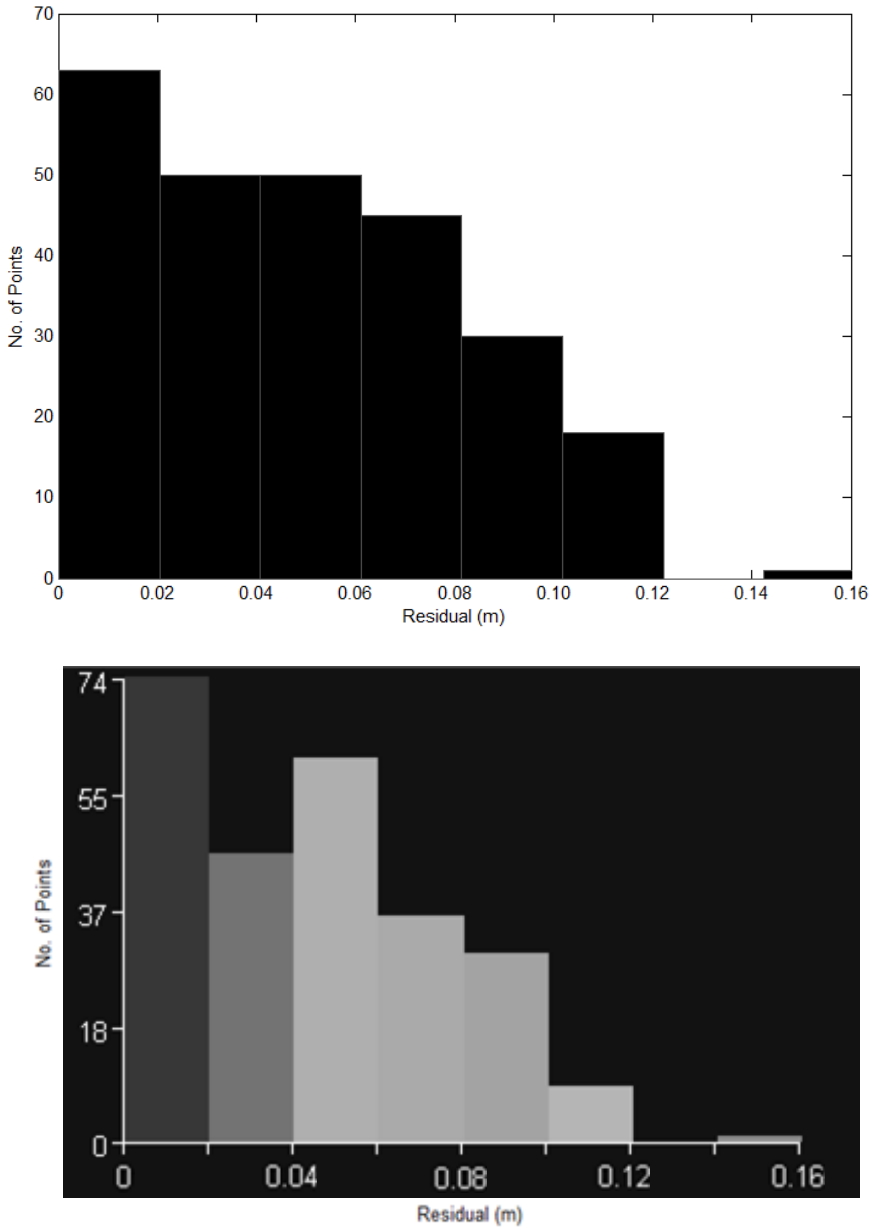

Figure 29: Typical histograms of point-to-plane (top) and point-to-point (bottom) residuals

This method was not as reliable as the first two approaches, as unrealistic distances can be calculated if the TLS pointcloud is not as dense as, or denser than, the MLS pointcloud. With sparse data, slant distances will be calculated in some areas instead of near-perpendicular dis-

tances (see Figure 30). This will cause the mean distance of the residuals to increase, generating a value that is larger than realistic. To overcome this, intensive quality control of selected planes would need to be considered to ensure that dense TLS data was used.

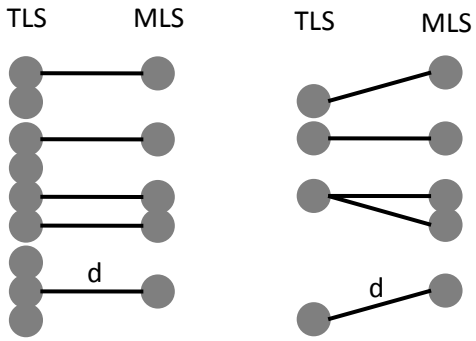

Figure 30: Nearest neighbor distances using dense TLS (left) and sparse TLS (right) data

To compare the three datasets and analysis methods, the RMS of the mean of the residuals from point-to-plane, and the RMS of the distances along the normal from the plane-to-plane method, were computed. Combining the plane means into one statistic provided an overall indicator of the accuracy level of the MLS system. Additionally, the simple RMS of the residuals from point-to-plane, the RMS of the mean of the unsigned residuals from point-to-plane, and the RMS of the mean of the residuals from the point-to-point method were determined. Residuals to vertical or horizontal planes were also determined separately for additional analysis (see Table 19 and Table 20).

Table 19: MLS to TLS planar patch comparison – I

	(m)	RMS Point-to-Plane Mean	RMS Plane-to-Plane Distance
Dataset 1	**Vertical Planes**	0.0639	0.0641
	Horizontal Planes	0.0305	0.0307
	All Planes	0.0492	0.0493
Dataset 2	**Vertical Planes**	0.0715	0.0718
	Horizontal Planes	0.0433	0.0176
	All Planes	0.0591	0.0532
Dataset 4	**Vertical Planes**	0.0445	0.0446
	Horizontal Planes	0.0413	0.0420
	All Planes	0.0415	0.0419
All Datasets	**Vertical Planes**	0.0613	0.0616
	Horizontal Planes	0.0387	0.0317
	All Planes	0.0505	0.0484

Table 20: MLS to TLS planar patch comparison – II

	(m)	RMS Point-to-Plane Residuals	RMS Point-to-Plane Unsigned Mean	RMS Point-to-Point Mean
Dataset 1	**Vertical Planes**	0.0810	0.0678	0.0727
	Horizontal Planes	0.0353	0.0321	0.0655
	All Planes	0.0651	0.0522	0.0690
Dataset 2	**Vertical Planes**	0.0899	0.0852	0.0908
	Horizontal Planes	0.0396	0.0708	0.0973
	All Planes	0.0640	0.0774	0.0933
Dataset 4	**Vertical Planes**	0.0608	0.0552	0.0601
	Horizontal Planes	0.0499	0.0441	0.0777
	All Planes	0.0574	0.0488	0.0692
All Datasets	**Vertical Planes**	0.0724	0.0709	0.0761
	Horizontal Planes	0.0402	0.0516	0.0812
	All Planes	0.0617	0.0608	0.0780

The results of Table 19 indicate the absolute accuracy of the system. The uncertainty between the MLS and TLS data is around ± 5 cm. Table 20 better demonstrates how noise affects the mapping-grade system results, and the difference between an absolute point position and its modeling ability. This will be discussed further in Section 5.1.2.3 and 5.1.2.4. Concisely, the first two calculations (Table 19) show how closely the data fits to the true position, and the last three (Table 20) demonstrate that noise is present. The point-to-point results are slightly larger, because they include possible errors in the TLS data as well. Nonetheless, all the methods still agree within a few centimeters.

An excellent use of the point-to-point comparison would be for examining complex surfaces that are not planes, because the errors in the control surface will be minimized. In Figure 31, a large building front with walls in multiple orientations, and a curved surface, is shown. Areas containing good TLS coverage were carefully selected to reduce point-to-point miscalculations. Here, the MLS points fit the TLS points with a mean of 0.050 ± 0.043 m. This is in closer agreement to the findings of the first two plane approaches. Two additional large surface features were selected and computed with means of 0.063 ± 0.036 m and 0.073 ± 0.035 m. Using the point-to-point approach on large varying surfaces rather than small planar patches produces similar and possibly better statistics, demonstrating a more appropriate use of this method.

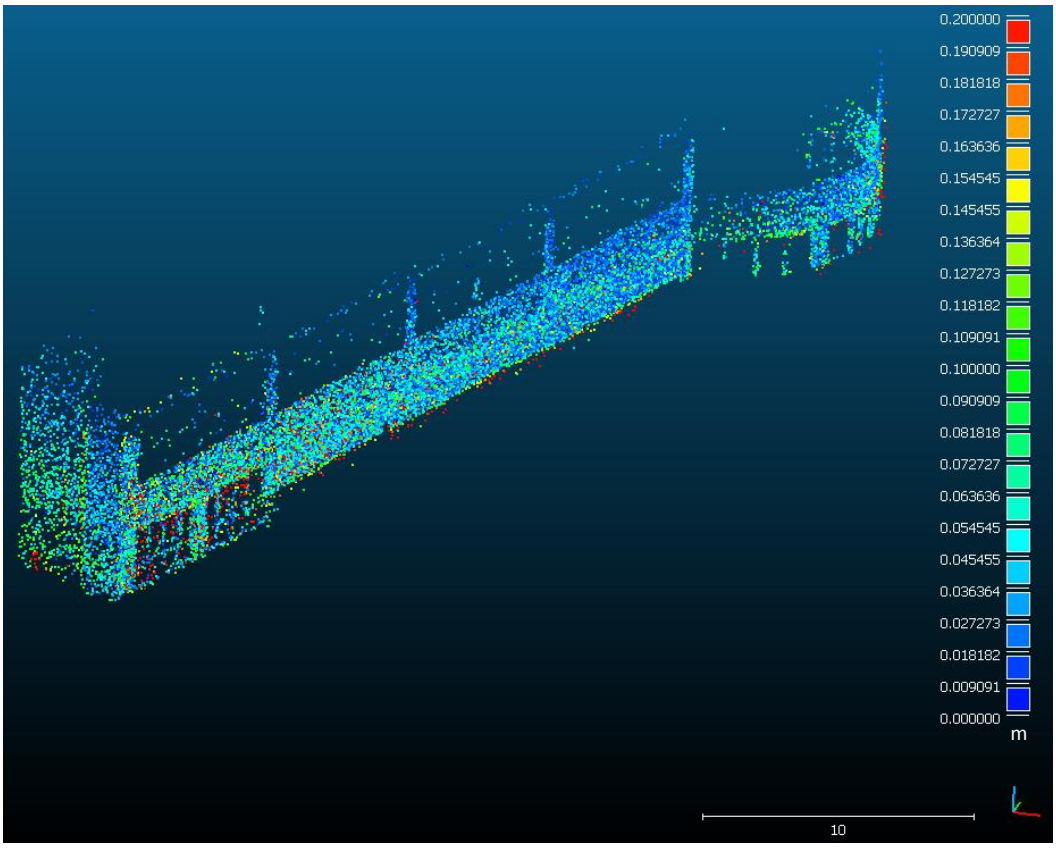

Figure 31: Point-to-point comparison of a large surface
(Distance from MLS point to TLS point shown by color scale)

Considering the results in Table 19 and Table 20, the three-dimensional accuracy of the MLS pointclouds are 4-8 cm. However, it can be seen that the horizontal planes, corresponding to vertical accuracy, are of higher accuracy than the vertical planes, which correspond to horizontal accuracy. These results are expected, as reported by Glennie (2007). The vertical accuracy is better by 25% or more than the horizontal accuracy. This is an improvement over the results initially stated in Glennie et al. (2013) with the MLS in balloon configuration, which is due to shorter average ranges in backpack mode. Likewise, the vertical accuracy is better because of shorter distances between the horizontal planes and instrument. This subject and its causes will be discussed with more detail in Section 5.3.

It can also be observed that the horizontal planes from the point-to-point method show higher RMS values than the vertical planes. This is opposite from the other approaches. This is the result of the TLS data being sparser and less evenly distributed in the horizontal planes because of the TLS instrument orientation and laser pattern geometry (refer to Figure 30 and the preceding discussion).

The results presented here demonstrate that the mapping-grade MLS system is viable for collecting topographic data and geological information, for corridor mapping and vegetation encroachment, and any other demand that falls within the required accuracy levels of 5-10 cm or greater. Using topographic data, change detection or deformation could be explored, and Digital Elevation Models (DEMs) or Digital Terrain Models (DTMs) could be built. In addition, extracting plane data for building footprints for Geographical Information System (GIS) maps is a viable option. More analysis on feature extraction ability is presented in Section 5.1.2.3.

5.1.2.2 Estimated v. Actual Error

Since the point-to-plane analysis is reasonably the best direct method to explore the accuracy of the MLS system, it is sensible to compare these values to the expected accuracy of the system reported as ± 15.5 cm in Section 2.1.3. The standard deviations of the residuals of the MLS points to their best-fit plane were used. The standard deviations corresponding to all 75 planes were below the estimated error, except three. They were statistically tested against the predicted error using a one-tailed χ^2-test (chi-squared test).

A χ^2-test was performed to compare a sample variance (planar error) against a population variance (estimated error). A one-tailed test was used since the only concern was when the sample variance was larger than the population variance. The statistical test was

Null Hypothesis, $H_0: S^2 = \sigma^2$ Alternate Hypothesis, $H_a: S^2 > \sigma^2$,

where

S^2 is the sample variance, given as the standard deviation squared, and

σ^2 is the population variance.

The null hypothesis was rejected when

$$\chi^2 > \chi^2_\alpha \,, \tag{7a}$$

where

χ^2 is the test statistic,

χ^2_α is the critical value, and

α is the level of significance.

The test statistic was the value at which the null hypothesis was rejected. It was given as

$$\chi^2 = \frac{\nu S^2}{\sigma^2} \,, \tag{7b}$$

where ν equals the degrees of freedom of the sample set. The critical value determines the statistical region of acceptance, determined by the level of significance. This subject is covered in greater depth in Ghilani (2010).

Considering each of the planes separately, all the planes failed to reject the null hypothesis, except two, at a 0.05 level of significance. This means that almost all the planes are statistically within the predicted accuracy at 95.0% confidence. This is encouraging, especially since most of the planar patch standard deviations fell well below the estimated accuracy.

5.1.2.3 Automated Feature Extraction

To assess the ability for useful features to be extracted from the MLS data, two semi-automated approaches were considered. Since most feature model development is done with software, an automated methodology is important. The pointclouds contain moderate noise, as seen in Table 18, but features are still easily recognizable when viewing them. For a pointcloud

to be valuable, however, information must be effectively extracted from it. The first features considered were line or edge features.

Using a software routine, 20 straight edge features, each around 3-4 m in length, were selected and automatically extracted from Dataset 1, along with ten features from each of the remaining two datasets. Equivalent features from both the TLS and MLS data were chosen. For clarification, linear features were where two surfaces of different orientations met and created an edge, such as a road, curb, or building corner.

Initial analysis can be made from observations of the extraction procedure. Because Dataset 2 and 4 had large instrument orientation zenith angles, the laser swath widths were much smaller, and therefore the data was sparser. This made it more difficult to extract edge features. If the data lacked density, a meandering line feature could be extracted where a straight edge was theoretically located. Also, several attempted edge selections in the datasets were not recognized by the software because of pointcloud noise. This is a detriment to the possible benefits of the MLS pointclouds. Likewise, only lines running parallel to the ground were extracted, because perpendicular lines contained too much noise. This was a result of poorer horizontal accuracy, as noted previously.

For a more tangible analysis, the point coordinates of the extracted edges in both the MLS and TLS data were used to calculate straight lines; best-fit lines were resolved using an SVD method (Shakarji 1998). Like the plane computations, residuals of the point to the line were computed and the statistics determined. Small TLS residuals indicated that straight lines were being used for analysis, and small MLS residuals showed an edge was actually extracted from the MLS pointcloud. Secondly, the angles between the lines were calculated as an ancillary check on the legitimacy of the two lines. Finally, the distances from the MLS points to the TLS

truth were determined. The RMS of the residuals was calculated, similar to the planar method (see Table 21).

Table 21: RMS of residuals of linear feature points to line equation

(m)	TLS Residuals	MLS Residuals	MLS v. TLS Edge
Dataset 1	0.0056	0.0152	0.0648
Dataset 2	0.0051	0.0147	0.0933
Dataset 4	0.0054	0.0181	0.0905
All Datasets	0.0054	0.0158	0.0794

A noticeable difference is present between the TLS truth and MLS data. This could be the result of a shift in the data, which will be discussed later, or due to pointcloud noise. As portrayed in Figure 32, an edge will be misrepresented and skewed if too much noise is present. This is unlike a planar feature, which can essentially overcome this problem by considering many points simultaneously.

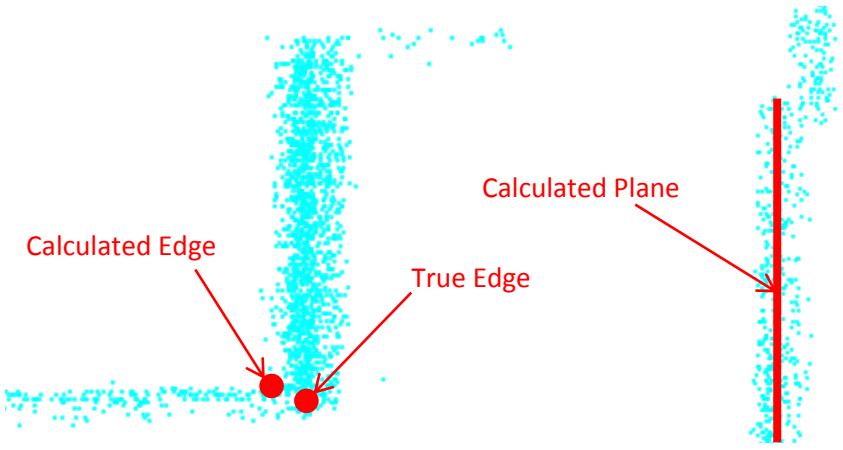

Figure 32: Software modeling ability with data containing noise

The residuals in Table 21 are unsigned distances. To determine if a shift was actually present, the perpendicular distance of the centroid of the MLS points to the TLS line was calculated. This is not as exacting as the first approach, but it is similar in theory to the plane-to-plane analysis. If MLS points were contained around the TLS line, the centroid to line distance should

be close to zero. As suspected, the RMS of the distances of the centroids to TLS lines were similar in magnitude to those found in Table 21, as well as being in agreement with the unsigned residuals found in the planar analysis in Table 20. This means there was a separation between the edge features of the MLS and TLS data. These statistics are tabulated in Table 22. Care should be taken when considering the datasets separately, because few features were selected for Dataset 2 and 4. The combination of all the datasets, however, provides a statistically significant value.

Table 22: Statistics of distances of MLS linear feature centroid to TLS line equation

(m)	Mean	Standard Deviation	RMS
Dataset 1	0.0550	0.0284	0.0616
Dataset 2	0.0807	0.0397	0.0890
Dataset 4	0.0750	0.0425	0.0852
All Datasets	0.0664	0.0362	0.0754

As far as extraction ability, the MLS results are about 3-4 times poorer than the TLS results, but still of excellent accuracy. This demonstrates the relative accuracy and modeling ability of the MLS system. Moreover, it should be remembered that the linear comparison between MLS and TLS is still within the expected accuracy of the system (see Section 2.1.3).

The semi-automated extraction of lines simulated the modeling of curbs, pavement edges, topographical breaklines, etc. (using a non-intensity method). With information such as this, road data can be created at an acceptable accuracy level for GIS mapping. This again verifies the ability of the system's pointcloud to provide building footprints. With a relative accuracy of less than ± 2 cm over a short time period, the MLS package can easily extract viable information. The data, however, must be dense enough, and the noise must be limited, for this method to be profitable.

The second automatic extraction analysis modeled cylindrical features in the point-clouds. Several concrete guard poles and utility poles in the survey area were used. Points of ten cylinders from both Dataset 1 and 2, and eight from Dataset 4, were selected in both the MLS and TLS pointclouds. From these, a model was estimated using Leica Cyclone software. The difference between the cylinder radius of TLS truth and MLS models were calculated (see Table 23). As is shown, the MLS agrees with the TLS at sub 3-cm levels. The modeled radii are nominally within 10% of the true values. This again shows the ability of the system in collecting useful feature information. Furthermore, *in situ* measurements were taken for comparison. First, this was a good opportunity to verify the TLS data. The field measurements were made to the nearest centimeter with a steel tape. Considering the estimated precision of the measurements was only 1-2 cm, the TLS and *in situ* results agreed well, with an RMS of ± 3 mm. Similarly, the subsequent comparison between the MLS and field measurements agreed with the MLS versus TLS results (see Table 23).

Table 23: RMS of differences between MLS and truth cylinder radii

(m)	MLS v. TLS	MLS v. *In Situ*
Dataset 1	0.0156	0.0167
Dataset 2	0.0224	0.0236
Dataset 4	0.0250	0.0235
All Datasets	0.0211	0.0213

Finally, the residuals of the individual points to the model cylinders were evaluated (see Table 24). Residuals of the MLS points were calculated to surfaces determined by both the TLS data and by the MLS data. This showed how well the objects in the pointcloud matched the truth data and verified the ability of the mapping-grade MLS to model and extract information of good relative precision. These numbers showed good fit and generally agreed with the magnitude of the residuals from the planar data. Again, since less than 20 features were selected for

each dataset, caution should be taken when making conclusions about a single set. But, the combination of all datasets is a statistically sound value that also considers temporal changes.

Table 24: RMS of residuals of MLS points to best-fit cylindrical surface

(m)	MLS v. MLS Cylinder	MLS v. TLS Cylinder
Dataset 1	0.0485	0.0663
Dataset 2	0.0418	0.0665
Dataset 4	0.0414	0.0710
All Datasets	0.0452	0.0675

The cylinder diameter depends on the points chosen, and therefore care must be taken in selection. However, these modeling techniques display how the system's pointclouds can be useful in modeling objects like tree trunks for forestry applications, along with determining tree diameter at breast height, and light or utility poles for urban modeling and asset management. As-built scenarios, involving oil and gas transportation pipelines, could easily be collected by this system with accurate results. This idea could also be extended to volumetric modeling of objects, estimating stockpile mass, and simple object reconstruction.

5.1.2.4 Manual Feature Extraction

The capability of a user to accurately interpret information from the MLS system pointcloud is also of interest. To analyze the ability for a user to manually decipher information from a pointcloud, control points from the MLS and TLS data were selected and compared, and feature measurements were made and analyzed. The manual point picking can contain user error, but careful attention was exercised to reduce this effect. Because of the sparser pointclouds of Dataset 2 and 4, only five features were gathered, along with ten features in Dataset 1. Several corners of objects and tops or bottoms of posts were chosen as control points. A point was des-

ignated in the TLS data, and the corresponding point picked in the MLS pointcloud. Points were selected several times and their coordinates averaged to best determine each MLS feature.

The distance between the MLS point coordinates and TLS control point was calculated. This offset was the error. Like the edge analysis, the existing noise easily resulted in error when picking control points, as the true corner could actually be contained within the noise of an apparent corner.

A discernible shift was again present in the data, although it was not equivalent in magnitude or direction throughout the entire dataset. Nevertheless, the shifts were over 75% in one direction, with a standard deviation in the shifts of the individual coordinates of 5-7 cm. This shift was most likely due to processing errors and errors in lever-arm estimations, which can be reduced by processing experience and improved project planning and quality assurance.

The accuracy of target coordinate comparison, using the RMS of the distances, was 2-3 times poorer than the planar and automated analysis methods (see Table 25). When modeling planes and cylinders, an accumulation of points is used which reduces the overall noise. This effect, essentially the same concept presented in Figure 32, is not present in single point selection. Because of noise, varying density, and reduced object selection, this method was probably the least trustworthy approach to investigate the system's ability.

Table 25: Statistics of differences between MLS points and TLS control

(m)	Mean	Standard Deviation	RMS
Dataset 1	0.1252	0.0420	0.1313
Dataset 2	0.1680	0.0757	0.1811
Dataset 4	0.1082	0.0485	0.1166
All Datasets	0.1316	0.0552	0.1422

As mentioned, several dimensions in the pointcloud from the datasets were measured using pointcloud software. These features included stair landing insets, brick post widths and separations, loading dock widths and heights, ramp widths, railing lengths, and guard post heights. Measurements were taken several times and averaged. The measurements between the MLS and TLS data agreed reasonably well. They also matched the accuracy levels determined using the planar and cylinder analysis methods (see Table 26).

Table 26: RMS of differences between MLS measurements and truth

(m)	MLS v. TLS	MLS v. *In Situ*
Dataset 1	0.0367	0.032
Dataset 2	0.0530	0.057
Dataset 4	0.0476	0.041
All Datasets	0.0441	0.041

As in the preceding section, *in situ* measurements were made of the features. The TLS and *in situ* results had an RMS difference of ± 1.3 cm. The resulting comparison between the MLS and field measurements mirrored the MLS versus TLS results (see Table 26). The MLS measurements were nominally within 5% of the true values.

When comparing the results of Table 25 and Table 26, it can be seen that the relative accuracy of the pointcloud with manual extraction is more reliable than the absolute accuracy. The distances between object points show the absolute difference between the MLS and TLS data, while the object measurements show the relative precision. This is an important note to make. This also means any possible errors in scale are a minimum and contained within the noise.

Manual extraction methods can be used for making measurements on overpass and wire clearances or road widths. Building or object dimensions could also be taken effectively. The prime use is approximation of distances and locations for a user, within a few centimeters. If

corner points are needed to high accuracy, it is most viable to extract three planar surfaces and calculate the intersection as the corner of an object.

5.2 Mapping-Grade MLS v. Survey-Grade MLS

The mapping-grade system was compared to the survey-grade system to additionally assess its ability to collect accurate data. The survey-grade MLS system did not provide results as precise as the TLS scans because of the many contributing error sources. However, it was still highly reliable data. The survey-grade data represented the results from a typical MLS collection, hence the practicality of comparing the two systems.

The residuals of points to 25 planar patches were determined for the survey-grade data. Table 27 shows the RMS of the residuals to be only ± 1 cm. This is in agreement with the misclosure RMSE from the dataset's planar adjustment seen in Table 17, and shows that the survey-grade MLS data is a quality pointcloud to utilize as control data.

Table 27: Statistics from survey-grade MLS planar patch residuals

Mean (m)	0.0000
Unsigned Mean (m)	0.0071
RMS (m)	0.0101

Following the steps from Section 5.1.2.1, 25 planar surfaces were selected from each mapping-grade MLS dataset. The corresponding region in the survey-grade MLS data was also selected. The best-fit plane equation was determined for the survey-grade data, again using an SVD method. The residuals of the points from the mapping-grade planar patches to the control planes were computed (see Table 28). Once more, Dataset 1 exhibits the best results. The two systems are within 6-8 cm, agreeing with the conclusions found thus far.

Table 28: RMS of residuals from mapping-grade MLS points to survey-grade MLS plane

(m)	Vertical Planes	Horizontal Planes	All Planes
Dataset 1	0.0572	0.0631	0.0605
Dataset 2	0.0813	0.0624	0.0725
Dataset 4	0.0788	0.0561	0.0707
All Datasets	0.0732	0.0607	0.0675

For full comparison, the RMS of the point-to-plane mean and unsigned mean, the RMS of the plane-to-plane distance, and the RMS of the point-to-point mean were determined (see Table 29). Complete descriptions of the analysis methods are found in Section 5.1.2.1. The comparison methods produced RMS values of 5-8 cm. The results verified the findings of Table 28, as well as the previous conclusions. The reported results are slightly larger than determined by the TLS comparison (except for the point-to-point comparison). This is due to greater linear shifts in the pointclouds from additional errors present in the survey-grade MLS data not existing in the TLS data.

Table 29: Mapping-grade MLS to survey-grade MLS planar patch comparison

(m)	RMS Point-to-Plane Mean	RMS Plane-to-Plane Distance	RMS Point-to-Plane Unsigned Mean	RMS Point-to-Point Mean
Vertical Planes	0.0771	0.0785	0.0848	0.0806
Horizontal Planes	0.0475	0.0511	0.0563	0.0589
All Planes	0.0642	0.0664	0.0722	0.0707

These results demonstrate that the mapping-grade MLS system can collect useful data, but it is still not at the survey-grade level (less than ± 5 cm). As seen in Figure 33, the objects in the data collected by the survey-grade system are more easily distinguished than objects in the mapping-grade pointcloud. This is important, because the differences in level of detail deter-

mines for what purposes the systems can be effectively used. This also demonstrates the effect different qualities of laser scanners and IMUs have on an MLS system.

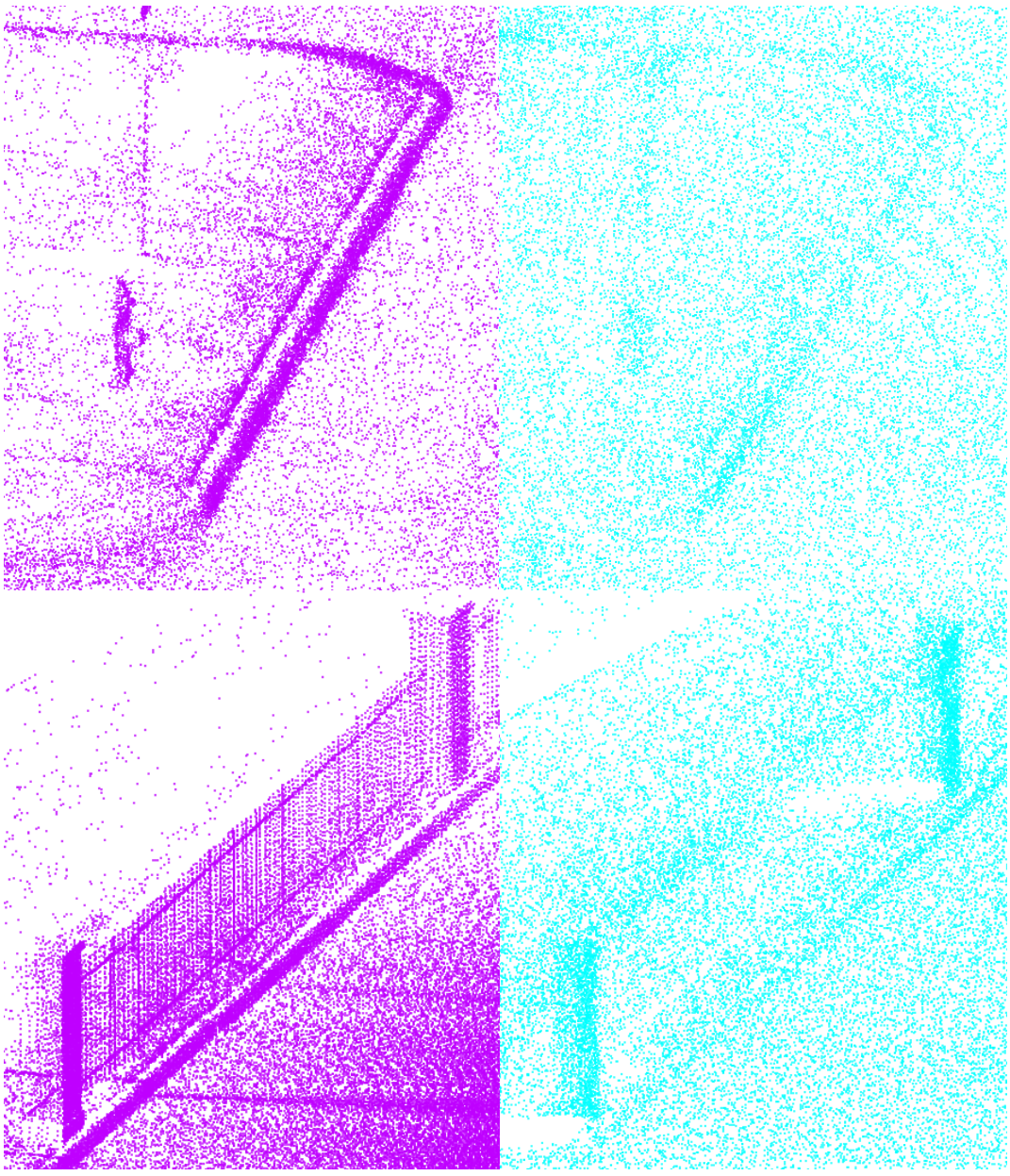

Figure 33: Pointcloud objects from survey-grade MLS data (left) and mapping-grade MLS data (right)

5.3 Laser Beam Divergence Contribution

The contribution to the error from the angle of incidence of the laser beam on a surface, as well as the range from instrument to object, are next explored to quantify their influence on overall system errors. The angle of incidence is described as the angle between a surface normal vector and laser vector. Using static LiDAR data similar to that of Section 4.3.1.1 for the Velodyne HDL-32E, a least-squares solution based on a planar model was used to fit planes to points. The residuals of over 300,000 points to 67 planes versus the angle of incidence and range were examined. The results are presented in Figure 34.

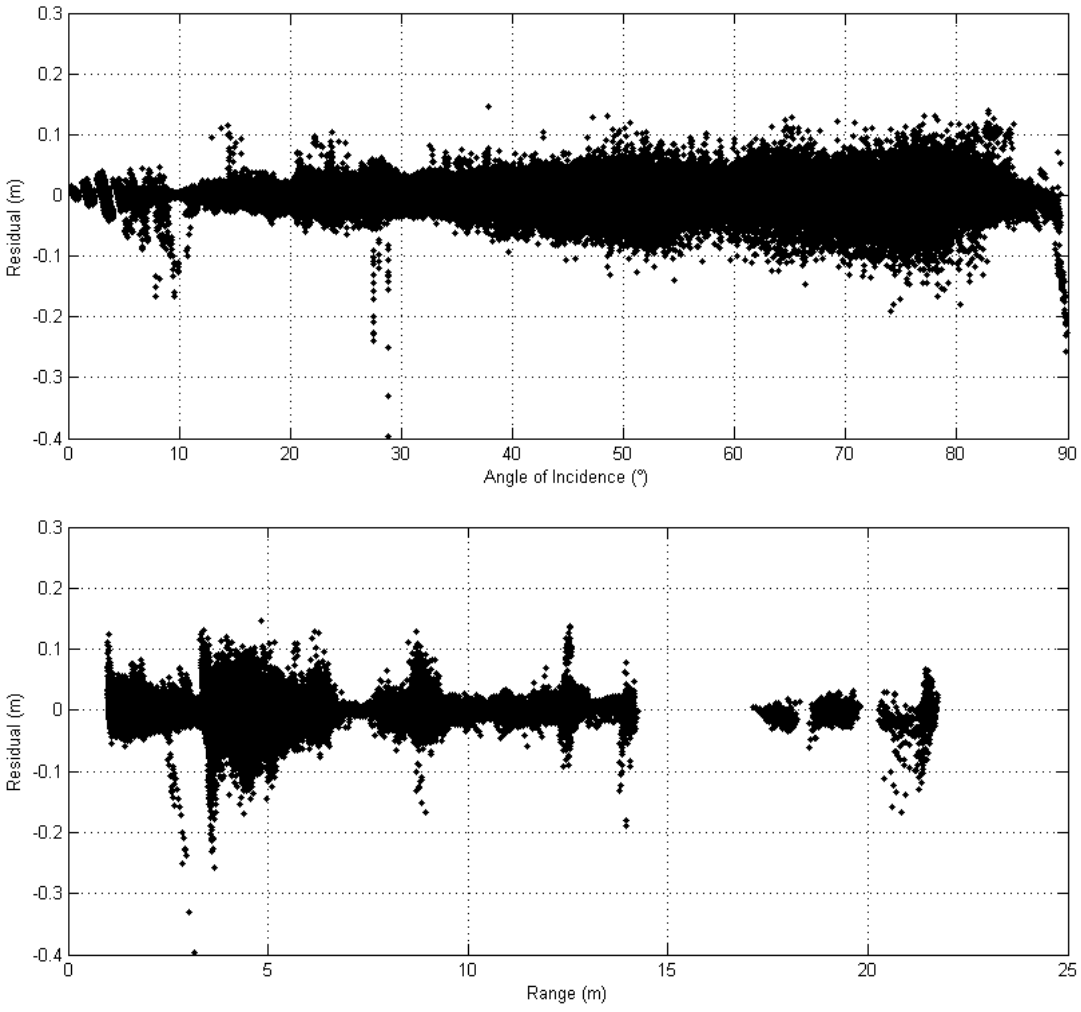

Figure 34: Effect of angle of incidence (top) and range (bottom) on point residuals for static collection of Velodyne HDL-32E

As can be seen graphically, the residual of a LiDAR point from a plane becomes larger as the angle of incidence increases. This result agrees with similar findings for Velodyne scanners in other comparable studies, given in Glennie and Lichti (2010). As the angle of incidence increases, the surface area illuminated by the beam will increase (see Figure 35). This will cause a discrepancy in the energy returned from the laser beam, because it will contain a combination of the reflections from the near and far edge of the beam footprint (Morin 2002, Petrie and Toth 2009b). Nevertheless, the return is always assumed to emanate from the center of the beam. This leads to errors in the estimated position of a point.

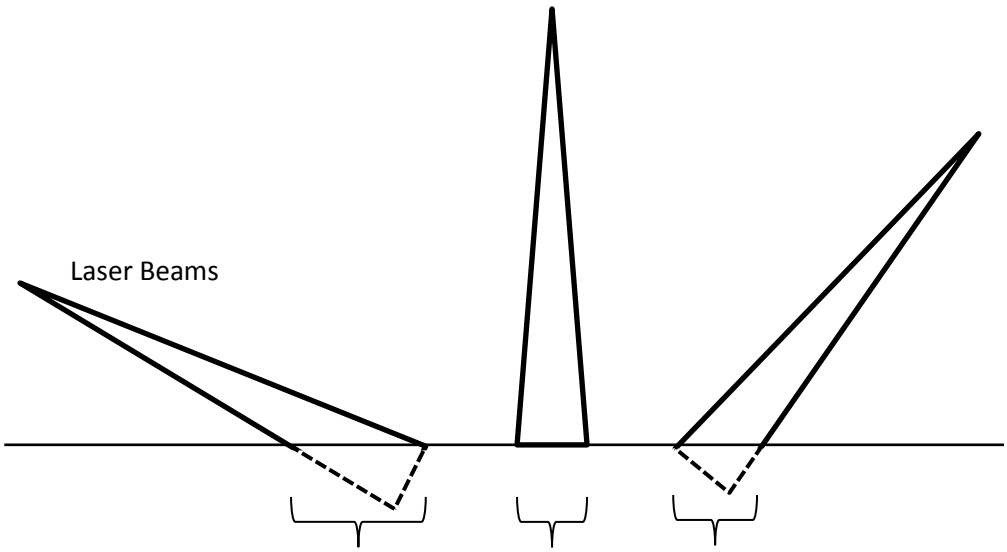

Figure 35: Surface area illumination from laser due to angle of incidence

In Figure 34, the maximum observed range was 22 m. In this case, the large residuals present in the range actually correspond to large incidence angles. As the distance to a target increases, beam divergence increases the size of the beam, as well. In the case of the Velodyne HDL-32E, the size of the beam footprint will be about 8 cm at 25 m. The position within the footprint is unknown but relies on the return energy and measures position as being along the beam's centerline, similar to above (Glennie 2007). The residuals in Figure 34 would be expected to increase due to range if the target distances increased to 50-70 m.

More important to MLS, are the errors present at long ranges due to IMU errors. As the distance to a target increases, any angular errors in the IMU measurements will increase proportionally to the range (Glennie 2007). This concept is demonstrated, using values from the mapping-grade MLS system, in Figure 36. The uncertainty due to the increase in the width of the laser beam is also included. In the MLS datasets presented, it is expected that both IMU angular error and beam divergence issues exist, since longer distances are present.

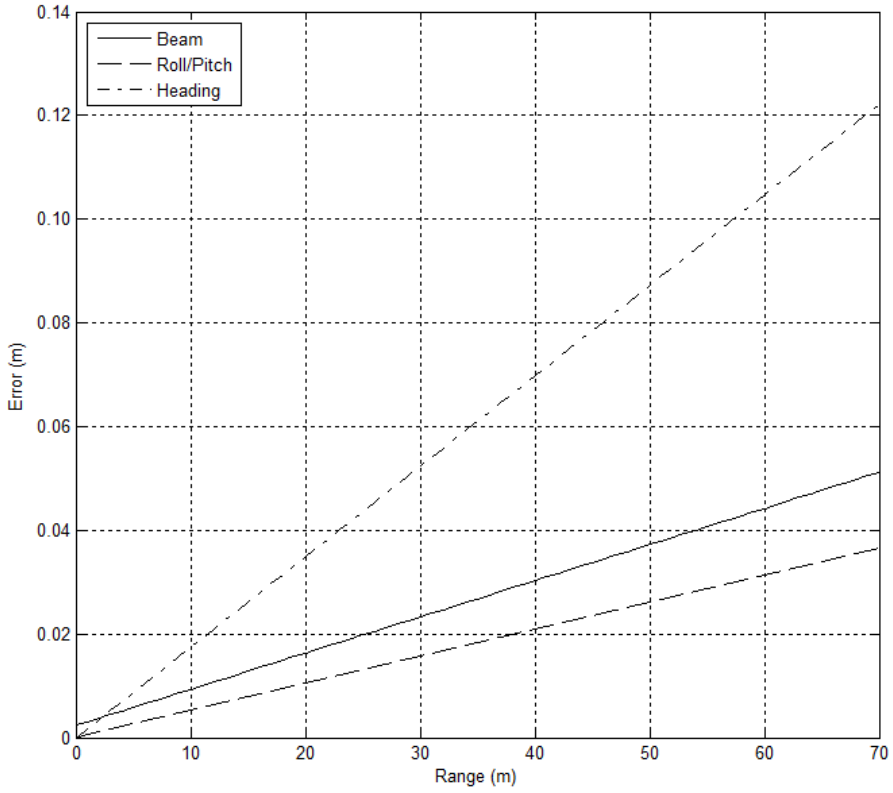

Figure 36: Theoretical point error due to beam divergence and IMU error

Revisiting the accuracy from the plane analysis in Section 5.1.2.1, an assessment can now be made as to why the horizontal accuracy is poorer than the vertical accuracy. Horizontal planes correspond to vertical accuracy, because the laser strikes a horizontal surface from a vertical direction. In this survey, the horizontal planes, while containing large incidence angles from the scanner orientation, were measured at short distances. The vertical planes, corresponding

to horizontal accuracy, consisted of longer ranges and larger beam divergences, yielding greater uncertainties and errors.

Additionally, some of the residuals in the cylinder calculations, or building edges, can be attributed to this. Although incidence angle and beam divergence did not greatly affect the overall ability of a cylinder to be modeled, as Table 23 and Table 24 demonstrate, it is visually evident (see Figure 37). Lichti et al. (2005) also report this effect.

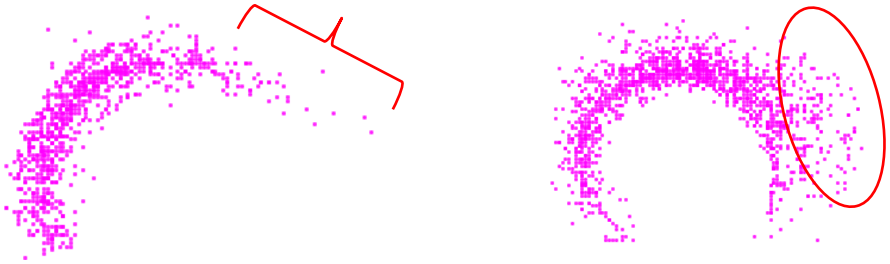

Figure 37: Point error due to beam divergence and incidence angle on a cylinder

Unfortunately, the errors mentioned in this section were difficult to directly examine in the mobile data. With several variables attributing to the error, including from the GNSS and INS, planar and cylindrical models did not consistently display the residuals from the angle of incidence or range, as was shown in Figure 34. The static examination, however, shows the significant effects these systematic errors can have, because they could be isolated from trajectory estimation errors.

5.4 Mapping-Grade MLS System Repeatability

It would be beneficial to verify the repeatability of the mapping-grade MLS system to collect quality data. To accomplish this, pointclouds from three locations using three collection techniques were compared. The assessment essentially considered the associated repeatability and noise level of the system results. This was done by analyzing point residuals to planes created with those points.

The first dataset was Dataset 1 from the previous analysis. Again, this was mobilized with a backpack. The second dataset was collected using the balloon mode on an island in Antioch, California (see Glennie et al. (2013)). The third dataset was obtained in a subdivision in Freemont, California, while mounted to a truck.

The new datasets were collected in a similar manner as discussed in Section 3, and likewise processed following the steps in Section 4. Twenty planar patches were selected from each pointcloud. A least-squares solution was computed for each plane, per Section 5.1.2.1, and the point-to-plane residuals for each point were determined. The RMS of the residuals was finally calculated (see Table 30).

Table 30: RMS of residuals from MLS points to plane

(m)	Vertical Planes	Horizontal Planes	All Planes
Houston	0.0462	0.0480	0.0457
Antioch	0.0582	0.3061	0.2299
Freemont	0.0385	0.0891	0.0604

Interesting results were discovered. In Table 30, the vertical planes were better than the horizontal planes. (The difference between vertical and horizontal for the Houston data was actually negligible, as the results can slightly change depending on the planes selected.) There could be several reasons for this. First, the scanner's field-of-view is approximately +10° to -30°. In the Houston dataset, the scanner was mounted about 10° from vertical; this means that the bottom laser was firing at 40° from horizontal. Assuming the system is scanning horizontal planes, the angle of incidence will be around 50°. Conversely, the scanner was mounted vertically, but upside down, while collecting the Freemont dataset. Using the same logic as above, the angle of incidence was approximately 80°. This is a significant change from the Houston dataset

and will have important effects on the precision of the horizontal planes, when considering the findings of Section 5.3. Regardless, the RMS is still within the bounds seen thus far.

The Antioch data show a significant decrease in reported precision, however. This is due to the observed ranges. The Houston and Freemont data contained nominal maximum ranges between 15-25 m, but the Antioch data, collected from a balloon with a flying height of approximately 25 m, had ranges between 30-45 m on the planar surfaces. The longer ranges cause the IMU errors and beam divergence to have greater consequence on the point uncertainty. Moreover, the dynamic range of angular rate of the OxTS Inertial+2 is ± 100°/$_s$. The platform exceeded this value numerous times, due to effects from wind, during the data collection. This would cause the IMU measurements to be unreliable and the resulting pointcloud accuracy to decrease significantly.

Additionally, because of the environment of the Antioch dataset, useful planar surfaces were much less available for analysis. Vertical surfaces contained a variety of orientations and elevations. This also caused many of the vertical surfaces to have short ranges to the instrument. The horizontal surfaces, on the contrary, were restricted in variety. All the horizontal surfaces were measured at a uniform range and were situated adjacent to one another. This could cause the vertical planes to be within expected repeatability limits and the horizontal planes to suffer. In this case, assumptions about the horizontal planes, and therefore vertical precision, should be made sparingly in the absence of more diverse data. It should finally be noted that, although the three-dimensional residuals of the Antioch data are large (± 23 cm), they are equivalent in magnitude to the predicted system errors determined by the analysis of Section 2.1.3. For the appropriate ranges, the uncertainty was expected to be over 20 cm (see Figure 12).

Overall, the results show similar magnitudes as the initial relative accuracy analysis. This is encouraging because each data collection was with unique operational conditions that could influence the overall accuracy. These included different deployment platforms, different environments and local obstructions, different operators, and different data processors. With the inclusion of this data, it is demonstrated that the mapping-grade MLS system can repeatedly and reliably collect data with precision levels of ± 10 cm or less.

6 CONCLUSIONS & DISCUSSION

A mapping-grade MLS system was built for adaptable use with a variety of platforms and flexibility for a diversity of environments. It used small, lightweight instruments, and had a relatively inexpensive cost. Because of the nature of the system, its accuracy is in question. It is important for all surveying instruments or systems to collect high-accuracy data, and the versatility of this MLS system makes knowing its performance ability essential.

Multiple datasets were collected and compared to high-accuracy TLS truth data. Additionally, the system's results were compared to a survey-grade MLS system containing significantly higher-accuracy components. The comparisons were promising and displayed the mapping-grade system's collection capability.

Planar features were used as the most basic method of comparing the pointclouds. Three basic methods were considered: point-to-plane, plane-to-plane, and point-to-point. Variations of these methods were included. The low-cost, mapping-grade MLS system agreed with the TLS on a level of 5-8 cm. This was well below the expected uncertainty of ± 15.5 cm (at 10 m). The same accuracy levels were found when comparing the mapping-grade MLS and survey-grade MLS systems.

Linear and cylindrical features were utilized to assess the mapping-grade system's pointcloud modeling ability. The MLS and TLS linear features agreed within 6-9 cm. All the cylindrical features were in agreement at approximately ± 7 cm, while the modeled radii of the cylinders were within 10-15% of their true values.

Control point comparisons and feature measurements were also made to evaluate the interpretability of the data. The object point coordinate comparison displayed the poorest results, showing agreements of ± 18 cm or less. This method, as previously discussed, was the least reliable assessment approach, but the results were still nominally within the overall pre-

dicted system uncertainty. Finally, the measured object features of the MLS system agreed with the true measurements to within 3-6 cm.

Based on the presented analysis, the three-dimensional accuracy of the system can be stated to be 6-8 cm. By examining the residuals of modeled features within the MLS pointclouds only, and the object measurement analysis, the relative accuracy of the system is ± 5 cm or better. Additionally, after comparing pointclouds from different surveys, it is indicated that the system can repeatedly collect data at the stated levels.

A majority of the analysis agreed well, but the best method for testing the system accuracy was calculating the RMS of the residuals of the MLS points to a plane determined from TLS. The TLS planar surfaces had little noise, and the plane equations were determined using least-squares. This provided a reliable truth value. Combining the residuals into one value provided the best approximation of the overall accuracy of the MLS plane, because an accumulation of points was compared against a single truth standard. The same concept was applied when determining the RMS of the point residuals to modeled cylindrical surfaces.

A few steps could be implemented to improve the accuracy of the mapping-grade MLS system. The most obvious action would be to reject points with high incidence angles and long ranges. This could significantly reduce the noise of the system. With the addition of collecting data in optimal GNSS conditions, it is believed that the system could collect and model data at the ± 5 cm level.

To conclude, some additional analysis could provide more insight into the system accuracy. Suggested future work includes extraction and comparison of extended curb or road features, instead of short, straight edges, as well as extraction of utility lines. It would be beneficial to examine the MLS data modeling ability of features with curvilinear or catenary characteris-

tics. Using different software packages for the extraction of the same features would also help confirm the results.

It would also be valuable to expand the analysis to complex surfaces. Varying natural surfaces or terrain could be compared by creating a DEM or DTM from both the MLS and TLS data. This would help better determine accuracy while using comprehensive regions of data. Further, analysis using truth models containing planes in multiple orientations, and the extraction of tree trunks to assess cylinders of varying size, could strengthen the results.

Since the error contribution of beam divergence due to range was limited, the static analysis should be extended utilizing longer ranges. More importantly, an attempt to study the point residuals with respect to angle of incidence and range, using a controlled mobile data collection, should be made. Likewise, this testing could specifically include consideration of GNSS outages and accuracy correlation to PDOP or trajectory quality – which was discussed but not quantified – through analysis of the pointclouds.

Because a majority of the comparison assessment was completed against TLS data, it would also be favorable to expand the evaluation versus the survey-grade MLS system. This could include advanced analysis, as done with the TLS data, instead of simply a planar comparison. Breaking slightly from the scope of this thesis, a separate side-by-side comparison of the individual sensors could exhibit more information on the potential accuracy of the system (i.e., HDL-32E v. VZ-400 or Inertial+2 v. LANDINS).

Future work for the mapping-grade MLS system itself should include upgrading the IMU (while still keeping costs low), reducing the system's weight, and simplifying the logging and computing capability. Platform testing should be done with a UAV focus, as well as adapting the system for indoor applications. Practical application studies should additionally be made using datasets collected by the system in the field.

Finally, the above analysis demonstrates the mapping-grade MLS system's ability to collect topographic data, including terrain, road, and structure location, as well as geological features. With careful collection techniques, the system can also provide data that will effectively model objects such as building walls, flat surfaces from bridges and other structures, poles, tree trunks, pipelines, curbs, overhead utility lines, etc. Basic engineering, structural, and architectural measurements can also be made with the MLS data.

Noting the nominal accuracy of ~8 cm, and the many possible uses of the data, the mapping-grade MLS system can be utilized in many engineering and Earth science applications. It is on the more accurate end of the mapping-grade system scale. This makes the system ideal for use in all but the highest-accuracy situations.

RESEARCH ACKNOWLEDGEMENTS

Support, through a research assistantship from the National Center for Airborne Laser Mapping (NCALM), through a grant from the National Science Foundation's (NSF) Division of Earth Sciences, Instrumentation and Facilities Program – EAR 1043051, and a teaching assistantship from the Cullen College of Engineering, at the University of Houston, are acknowledged. The purchase and development of the mapping-grade mobile laser scanning system was funded by the Public Interest Energy Research (PIER) program of the California Energy Commission, grant 500-09-035, to the School of Ocean and Earth Sciences and Technology at the University of Hawaii. Todd Ericksen and Jon Avery, of the University of Hawaii, are recognized for designing the instrument platform and integration of the system components.

REFERENCES

Baltsavias, E. P. "Airborne Laser Scanning: Basic Relations and Formulas." *ISPRS Journal of Photogrammetry and Remote Sensing*, 1999a: 199-214.

Baltsavias, E. P. "Airborne Laser Scanning: Existing Systems and Firms and Other Resources." *ISPRS Journal of Photogrammetry and Remote Sensing*, 1999b: 164-198.

Barber, David, Jon Mills, and Sarah Smith-Voysey. "Geometric Validation of a Ground-Based Mobile Laser Scanning System." *ISPRS Journal of Photogrammetry and Remote Sensing*, 2008: 128-141.

Beraldin, J.-Angelo, Francois Blais, and Uwe Lohr. "Laser Scanning Technology." In Airborne and Terrestrial Laser Scanning, by George Vosselman and Hans-Gerd Maas, 1-42. Scotland: Whittles Publishing, 2010.

Boehler, W., M. Bordas Vicent, and A. Marbs. "Investigation Laser Scanner Accuracy." *International Archives of Photogrammetry, Remote Sensing and Spatial Information Sciences.* Antalya: ISPRS, 2003. 696-701.

Brooks, Benjamin A., Craig Glennie, Kenneth W. Hudnut, Todd Ericksen, and Darren Hauser. "Mobile Laser Scanning Applied to the Earth Sciences." *Eos, Transactions American Geophysical Union*, n.d.: (Accepted Pending Revision).

Carter, William E., Ramesh L. Shrestha, and K. Clint Slatton. "Geodetic Laser Scanning." *Physics Today*, December 2007: 41-47.

Carter, William, Ramesh Shrestha, Grady Tuell, David Bloomquist, and Michael Sartori. "Airborne Laser Swath Mapping Shines New Light on Earth's Topography." *Eos, Transactions American Geophysical Union*, November 13, 2001: 549-564.

Chase, Arlen F., Diane Z. Chase, John F. Weishampel, Jason B. Drake, Ramesh L. Shrestha, K. Clint Slatton, Jaime J. Awe, and William E. Carter. "Airborne LiDAR, Archaeology, and the

Ancient Maya Landscape at Caracol, Belize." *Journal of Archaeological Science*, 2011: 387-398.

Devereux, B. J., G. S. Amable, P. Crow, and A. D. Cliff. "The Potential of Airborne Lidar for Detection of Archaeological Features Under Woodland Canopies." *Antiquity*, 2005: 648-660.

Ellum, C. M., and N. El-Sheimy. "Land-Based Integrated Systems for Mapping and GIS Applications." *Survey Review*, 2002: 323-339.

El-Sheimy, N., and K. P. Schwarz. "Kinematic Positioning in Three Dimensions Using CCD Technology." *Proceedings of the IEEE/IEE Vehicle Navigation and Information Systems Conference 1993.* Ottawa: IEEE, 1993. 472-475.

Ghilani, Charles D. Adjustment Computations: Spatial Data Analysis. Hoboken: John Wiley and Sons, Inc., 2010.

Glennie, Craig. "Calibration and Kinematic Analysis of the Velodyne HDL-64E S2 Lidar Sensor." *Photogrammetric Engineering and Remote Sensing*, 2012: 339-347.

Glennie, Craig. "Kinematic Terrestrial Light-Detection and Ranging System for Scanning." *Transportation Research Record: Journal of the Transportation Research Board*, 2009: 135-141.

Glennie, Craig. "Rigorous 3D Error Analysis of Kinematic Scanning LIDAR Systems." *Journal of Applied Geodesy*, 2007: 147-157.

Glennie, Craig, and Derek D. Lichti. "Static Calibration and Analysis of the Velodyne HDL-64E S2 for High Accuracy Mobile Scanning." *Remote Sensing*, 2010: 1610-1624.

Glennie, Craig, and Derek D. Lichti. "Temporal Stability of the Velodyne HDL-64E S2 Scanner for High Accuracy Scanning Applications." *Remote Sensing*, 2011: 539-553.

Glennie, Craig, Benjamin Brooks, Todd Ericksen, Darren Hauser, Kenneth Hudnut, James Foster, and Jon Avery. "Compact Multipurpose Mobile Laser Scanning System - Initial Tests and Results." *Remote Sensing*, 2013: 521-538.

Goad, Clyde C. "The Ohio State University Highway Mapping Project: The Positioning Component." *Proceedings of the 47th Annual Meeting of The Institute of Navigation.* Williamsburg: ION, 1991. 117-120.

Grejner-Brzezinska, Dorota A. "Mobile Mapping Technology: Ten Years Later (Part One)." *Surveying and Land Information Systems*, 2001: 75-91.

Groves, Paul D. Principles of GNSS, Inertial, and Multisensor Integrated Navigation Systems. Boston: Artech House, 2008.

Guenther, Gary C. "Airborne Lidar Bathymetry." In Digital Elevation Model Technologies and Applications: The DEM Users Manual, by David F. Maune, 253-320. Bethesda: ASPRS, 2007.

Haala, Norbert, Michael Peter, Jens Kremer, and Graham Hunter. "Mobile LIDAR Mapping for 3D Point Cloud Collection in Urban Areas - A Performance Test." *The International Archives of the Photogrammetry, Remote Sensing and Spatial Information Sciences.* Beijing: ISPRS, 2008. 1119-1124.

Hecht, Jeff. "Short History of Laser Development." *Optical Engineering*, 2010: 091002.

Hofmann-Wellenhof, Bernhard, Herbert Lichtenegger, and Elmar Wasle. GNSS - Global Navigation Satellite Systems: GPS, GLONASS, Galileo and More. Vienna: Springer-Verlag Wien, 2008.

Hunter, G., C. Cox, and J. Kremer. "Development of a Commercial Laser Scanning Mobile Mapping System - StreetMapper." *The International Archives of the Photogrammetry, Remote Sensing and Spatial Information Sciences.* Antwerp: ISPRS, 2006.

Jaakkola, Anttoni, Juha Hyyppa, Antero Kukko, Xiaowei Yu, Harri Kaartinen, Matti Lehtomaki, and Yi Lin. "A Low-Cost Multi-Sensoral Mobile Mapping System and its Feasibility for Tree Measurements." *ISPRS Journal of Photogrammetry and Remote Sensing*, 2010: 514-522.

Jochem, Andreas, Bernhard Hofle, and Martin Rutzinger. "Extraction of Vertical Walls from Mobile Laser Scanning Data for Solar Potential Assessment." *Remote Sensing*, 2011: 650-667.

Lato, M., J. Hutchinson, M. Diederichs, D. Ball, and R. Harrap. "Engineering Monitoring of Rockfall Hazards Along Transportation Corridors: Using Mobile Terrestrial LiDAR." *Natural Hazards and Earth System Sciences*, 2009: 935-946.

Lichti, Derek D., Stuart J. Gordon, and Taravudh Tipdecho. "Error Models and Propagation in Directly Georeferenced Terrestrial Laser Scanner Networks." *Journal of Surveying Engineering*, 2005: 135-142.

Lichti, Derek, and Jan Skaloud. "Registration and Calibration." In Airborne and Terrestrial Laser Scanning, by George Vosselman and Hans-Gerd Maas, 83-133. Scotland: Whittles Publishing, 2010.

Lin, Yi, Anttoni Jaakkola, Juha Hyyppa, and Harri Kaartinen. "From TLS to VLS: Biomass Estimation at Individual Tree Level." *Remote Sensing*, 2010: 1864-1879.

Lin, Yi, Juha Hyyppa, and Anttoni Jaakkola. "Combining Mobile and Static Terrestrial Laser Scanners to Investigate Individual Crown Attributes During Foliation." *Canadian Journal of Remote Sensing*, 2011: 359-375.

Lindenbergh, Roderik. "Engineering Applications." In Airborne and Terrestrial Laser Scanning, by George Vosselman and Hans-Gerd Maas, 237-269. Scotland: Whittles Publishing, 2010.

Maybeck, Peter S. Stochastic Models, Estimation, and Control: Volume 1. New York: Academic Press, Inc., 1979.

Morin, Kristian Walker. Calibration of Airborne Laser Scanners. Master of Science Thesis, Calgary: University of Calgary, 2002.

Nagai, Masahiko, Tianen Chen, Ryosuke Shibasaki, Hideo Kumagai, and Afzal Ahmed. "UAV-Borne 3D Mapping System by Multisensor Integration." *IEEE Transactions on Geoscience and Remote Sensing*, 2009: 701-708.

Newby, Simon, and Paul Mrstik. "LiDAR on the Level in Afghanistan." *GPS World*, July 2005: 16-22.

Novak, Kurt. "The Ohio State University Highway Mapping System: The Stereo Vision System Component." *Proceedings of the 47th Annual Meeting of The Institute of Navigation.* Williamsburg: ION, 1991. 121-124.

Olsen, Michael J., Gene V. Roe, Craig Glennie, Fred Persi, Marcus Reedy, David Hurwitz, Keith Williams, Halston Tuss, Anthony Squellati, and Michael Knodler. Guidelines for the Use of Mobile LIDAR in Transportation Applications. NCHRP Report, Washington, DC: National Academy of Sciences, 2013.

Petrie, Gordon, and Charles K. Toth. "Airborne and Spaceborne Laser Profilers and Scanners." In Topographic Laser Ranging and Scanning: Principles and Processing, by Jie Shan and Charles K. Toth, 29-85. Boca Raton: Taylor and Francis Group, LLC, 2009a.

Petrie, Gordon, and Charles K. Toth. "Introduction to Laser Ranging, Profiling, and Scanning." In Topographic Laser Ranging and Scanning: Principles and Processing, by Jie Shan and Charles K. Toth, 1-27. Boca Raton: Taylor and Francis Group, LLC, 2009b.

Petrie, Gordon, and Charles K. Toth. "Terrestrial Laser Scanners." In Topographic Laser Ranging and Scanning: Principles and Processing, by Jie Shan and Charles K. Toth, 87-127. Boca Raton: Taylor and Francis Group, LLC, 2009c.

Puente, I., H. Gonzalez-Jorge, B. Riveiro, and P. Arias. "Accuracy Verification for the Lynx Mobile Mapper System." *Optics and Laser Technology*, 2013a: 578-586.

Puente, I., H. Gonzalez-Jorge, J. Martinez-Sanchez, and P. Arias. "Review of Mobile Mapping and Surveying Technologies." *Measurement*, 2013b: 2127-2145.

Rieger, P., N. Studnicka, M. Pfennigbauer, and G. Zach. "Boresight Alignment Method for Mobile Laser Scanning Systems." *Journal of Applied Geodesy*, 2010: 13-21.

RIEGL. "RiSCAN PRO: Technical Documentation and Users Instructions." RIEGL LMS, 2011.

Schwarz, Charles R., Richard A. Snay, and Tomas Soler. "Accuracy Assessment of the National Geodetic Survey's OPUS-RS Utility." *GPS Solutions*, 2009: 119-132.

Schwarz, K. P., H. E. Martell, N. El-Sheimy, R. Li, M. A. Chapman, and D. Cosandier. "VIASAT - A Mobile Highway Survey System of High Accuracy." *Proceedings of the IEEE/IEE Vehicle Navigation and Information Systems Conference 1993.* Ottawa: IEEE, 1993. 476-481.

Shakarji, Craig M. "Least-Squares Fitting Algorithms of the NIST Algorithm Testing System." *Journal of Research of the National Institute of Standards and Technology*, 1998: 633-641.

Shrestha, R. L., W. E. Carter, M. Sartori, B. J. Luzum, and K. C. Slatton. "Airborne Laser Swath Mapping: Quantifying Changes in Sandy Beaches Over Time Scales of Weeks to Years." *ISPRS Journal of Photogrammetry and Remote Sensing*, 2005: 222-232.

Snay, Richard, Kevin Choi, Gerald Mader, Charles Schwarz, Tomas Soler, and Neil Weston. "How Precise is OPUS? Part 3: The Rest of the Story." *The American Surveyor*, 2011: 42-46.

Soler, T., P. Michalak, N. D. Weston, R. A. Snay, and R. H. Foote. "Accuracy of OPUS Solutions for 1- to 4-h Observing Sessions." *GPS Solutions*, 2005: 45-55.

Titterton, David H., and John L. Weston. Strapdown Inertial Navigation Technology. Stevenage: The Institution of Electrical Engineers, 2004.

Vaaja, Matti, Juha Hyyppa, Antero Kukko, Harri Kaartinen, Hannu Hyyppa, and Petteri Alho. "Mapping Topography Changes and Elevation Accuracies Using a Mobile Laser Scanner." *Remote Sensing*, 2011: 587-600.

Wallace, Luke, Arko Lucieer, Christopher Watson, and Darren Turner. "Development of a UAV-LiDAR System with Application to Forest Inventory." *Remote Sensing*, 2012: 1519-1543.

Yen, Kin S., Kevin Akin, Arvern Lofton, Bahram Ravani, and Ty A. Lasky. Using Mobile Laser Scanning to Produce Digital Terrain Models of Pavement Surfaces. Caltrans Report, Davis: AHMCT Research Center, 2010.

Young, Adam P., M. J. Olsen, N. Driscoll, R. E. Flick, R. Gutierrez, R. T. Guza, E. Johnstone, and F. Kuester. "Comparison of Airborne and Terrestrial Lidar Estimates of Seacliff Erosion in Southern California." *Photogrammetric Engineering and Remote Sensing*, 2010: 421-427.